J. Fluid Mech. (2008), *vol.* 598, *pp.* 293–319.
doi:10.1017/S0022112007009949 Printed in the United Kingdom

Spiral swimming of an artificial micro-swimmer

ERIC E. KEAVENY AND MARTIN R. MAXEY

Division of Applied Mathematics, Brown University, 182 George Street, Box F, Providence, RI 02912, USA

(Received 10 May 2007 and in revised form 8 November 2007)

A device constructed from a filament of paramagnetic beads connected to a human red blood cell will swim when subject to an oscillating magnetic field. Bending waves propagate from the tip of the tail toward the red blood cell in a fashion analogous to flagellum beating, making the artificial swimmer a candidate for studying what has been referred to as 'flexible oar' micro-swimming. In this study, we demonstrate that under the influence of a rotating field the artificial swimmer will perform 'corkscrew'-type swimming. We conduct numerical simulations of the swimmer where the paramagnetic tail is represented as a series of rigid spheres connected by flexible but inextensible links. An optimal range of parameters governing the relative strength of viscous, elastic and magnetic forces is identified for swimming speed. A parameterization of the motion is extracted and examined as a function of the driving frequency. With a continuous elastica/resistive force model, we obtain an expression for the swimming speed in the low-frequency limit. Using this expression we explore further the effects of the applied field, the ratio of the transverse field to the constant field, and the ratio of the radius of the sphere to the length of the filament tail on the resulting dynamics.

1. Introduction

Low-Reynolds-number flows are kinematically reversible, and, accordingly, to generate a net translation a micro-swimmer's cyclic strategy must be one that is non-reciprocal (Purcell 1977). Many of the single cell micro-organisms that propel themselves in this environment utilize a long flagellum tail connected to the cell body. Purcell categorizes the majority of these flagella or one-armed swimmers as either those that use a 'flexible oar' strategy, or a 'corkscrew' strategy. The 'flexible oar' swimmers, such as spermatozoa, swim by propagating bending waves down the length of their flagellum tail, while swimmers applying the 'corkscrew' strategy, such as *E. coli* bacteria, rotate their helically shaped flagellum or flagellar bundles which afford the conversion of rotational to translational motion.

Beginning with G. I. Taylor's study of a swimming sheet (Taylor 1951) and subsequent analysis concerning motions associated with waves generated along a cylindrical tail (Taylor 1952), the development of model systems has been essential to understanding the fundamental principles surrounding the swimming of micro-organisms. Recent investigations that keep with this approach include studies of Purcell's three-link swimmer (Purcell 1977; Becker, Koehler & Stone 2003) and the measurements of the lateral force generated by filament when one end is displaced transversely in an oscillatory manner (Wiggins *et al.* 1998; Yu, Lauga & Hosoi 2006; Lauga 2007). A promising candidate for an additional model system is the artificial magnetic micro-swimmer produced by Dreyfus *et al.* (2005).

The artificial swimmer consists of a flexible magnetic flagellum-like tail connected to a human red blood cell. The red blood cell provides the asymmetry necessary for swimming to occur. The magnetic filament comprises spherical micron-sized paramagnetic beads linked together by DNA molecules. To form the filament, the paramagnetic beads are allowed to aggregate under the influence of a uniform magnetic field, forming chains aligned with the applied field (Promislow, Gast & Fermigier 1995). The surfaces of the beads are chemically treated so, when introduced, the DNA molecules bind the self-assembled beads together. The elastic properties of such filaments have been studied by Goubault *et al.* (2003) and Biswal & Gast (2003) and used as a key component of a mixing device by Biswal & Gast (2004).

Driving the motion of the swimmer is the oscillatory magnetic field of the form

$$\boldsymbol{H} = -H_0\,(1, h_0 \sin \omega t, 0)\,. \tag{1.1}$$

The competing magnetic forces and viscous stresses induce bending waves that travel from the tip of the filament tail and towards the red blood cell. In this study, we demonstrate the artificial micro-swimmer can also be used to study corkscrew-type swimming. When driven by the field

$$\boldsymbol{H} = -H_0\,(1, h_0 \sin \omega t, h_0 \cos \omega t)\,, \tag{1.2}$$

the balance of the magnetic, viscous and elastic forces cause the swimmer to take on a spiral shape. Additionally, the swimmer will rotate at the same frequency as the applied field, and therefore, translate through the fluid.

Two distinct models are adopted to describe the behaviour of a swimmer constructed from a magnetic filament tethered to a large rigid sphere. The first model is a particle-based approach presented in § 2, where the filament tail is treated as a series of rigid spheres joined by flexible, but inextensible links. The parameters for bead size and chain length may therefore be matched to experimental conditions. Additionally, the three-dimensional bending of each individual chemically formed link is accounted for. The particle-based representation also allows for mutual magnetic dipole interactions. A higher-order representation of the hydrodynamic forces is provided by the force-coupling method (FCM) (Maxey & Patel 2001; Lomholt & Maxey 2003). The inclusion of these features goes beyond the description employed by Gauger & Stark (2006) to study the swimmer under planar actuation where the beads comprising the tail interacted magnetically through fixed dipole interactions and experienced fluid forces based on the Rotne–Prager mobility. Additionally, the resistance to bending was represented by a wormlike chain: see Lagomarsino, Pagonabarraga & Lowe (2005) and Lowe (2003). The results from our particle-based simulations are presented in § 3, from which the kinematics of the swimmer's motion are deduced and analysed. The variation of the swimming speed with the frequency of the applied field is examined.

Along with the particle-based description and simulations, we consider a model where the magnetic filament tail is treated as a continuous elastica subject to magnetic torques and hydrodynamic drag. These simplifications yield a model that includes the features essential to the motion, but is still accessible to analysis. This allows us to explore further the parameters governing the swimming speed and make comparisons with the more realistic particle-based simulations. Elastica models, in combination with slender body theory for the hydrodynamic forces, have been the basis of a number of studies including the discussion by Dreyfus *et al.* (2005) of their experiments with the artificial swimmer, and by Cebers & Javaitis (2004*a*), Cebers & Javaitis (2004*b*) and Cebers (2006) for magnetic filaments in rotating fields and shear flows. In § 4,

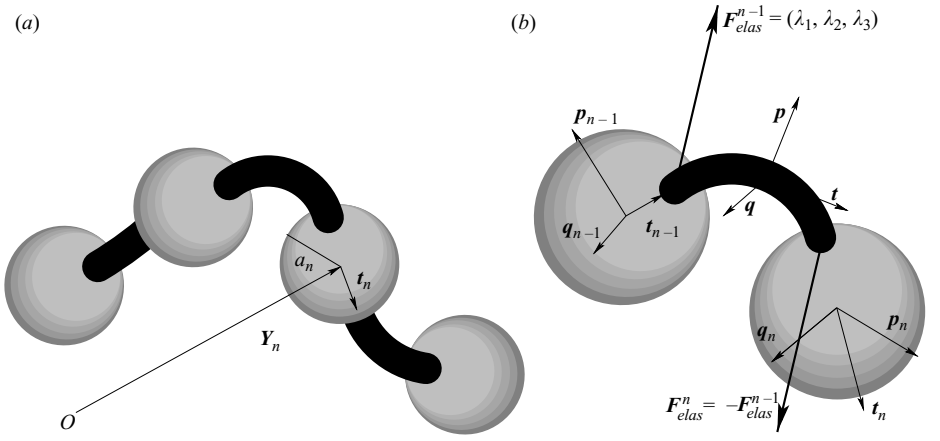

FIGURE 1. (*a*) Sketch of a section of the magnetic filament tail showing the position, $\boldsymbol{Y}_n$, radius a_n, and the unit vector $\boldsymbol{t}_n$ for bead n. The vector $\boldsymbol{t}_n$ points from the particle's centre to the attachment point of the link. (*b*) Sketch of two neighbouring particles of the filament. The link exerts a force $\boldsymbol{F}^{n-1}_{elas}$ on bead $n-1$ and an equal and opposite force on bead n. The shape of the link is characterized by the coordinate system $(\boldsymbol{t}, \boldsymbol{p}, \boldsymbol{q})$ that varies along the length and attains values $(\boldsymbol{t}_{n-1}, \boldsymbol{p}_{n-1}, \boldsymbol{q}_{n-1})$ at the left attachment point, and $(\boldsymbol{t}_n, \boldsymbol{p}_n, \boldsymbol{q}_n)$ at the opposite end.

we extend the model of Roper *et al.* (2006) used in their study of magnetically driven elastic filaments to include fully three-dimensional motion and a higher-level representation of the magnetic interactions. An analysis of spiral swimming at low frequency is then given in § 5.

2. Simulation methods

In the particle-based approach, the magnetic swimmer is treated as a series of $N+1$ rigid spheres, where the first N beads are paramagnetic and comprise the filament tail. Bead $N+1$ is a large, non-paramagnetic sphere and provides a representation of the artificial swimmer's red blood cell cargo (Dreyfus *et al.* 2005). Each bead $n = 1 \ldots N+1$ centred at $\boldsymbol{Y}_n$ has local body axes $(\boldsymbol{t}_n, \boldsymbol{p}_n, \boldsymbol{q}_n)$ and is of radius a_n, where $a_n = a$ for the paramagnetic spheres $n = 1 \ldots N$ and $a_{N+1} = R$ for the large sphere (figure 1*a*). In the experiments, the ratio $R/a \approx 6.0$ (Dreyfus *et al.* 2005). The unit vector $\boldsymbol{t}_n$ is defined such that the locations of points on the surface of sphere n where the two links are attached are $\boldsymbol{Y}_n \pm a_n \boldsymbol{t}_n$. Additionally, magnetic beads comprising the tail have magnetic permeability μ. The permeability of the surrounding medium is taken to be that of free space μ_0.

In the experiments, the paramagnetic beads are of radius $a = 0.5\,\mu\text{m}$ and a typical frequency of the applied field is $\omega = 62.8\,\text{rad}\,\text{s}^{-1}$ (Dreyfus *et al.* 2005). With the viscosity of the surrounding fluid, η, being that of water, the Reynolds number corresponding to the motion is $Re = \rho\omega a^2/\eta \approx 10^{-5}$ (Roper *et al.* 2006). Under the conditions for low-Reynolds-number Stokes flow, the resulting magnetic, hydrodynamic and elastic forces and the hydrodynamic and elastic torques on the beads are, at any instant, in equilibrium,

$$\boldsymbol{F}^n_{hydro} + \boldsymbol{F}^n_{mag} + \boldsymbol{F}^n_{elas} = 0, \tag{2.1}$$

$$\boldsymbol{\tau}^n_{hydro} + \boldsymbol{\tau}^n_{elas} = 0, \tag{2.2}$$

for $n = 1 \ldots N$. The force and torque balance for $n = N + 1$ is the same, except that there are no magnetic forces to consider.

Neglected in the force and torque balances are the effects of thermal fluctuations. One might imagine a situation where Brownian motion may have a significant impact on the motion of the micron-sized paramagnetic beads. In this context, the relative importance of these effects is provided by the parameter

$$\Lambda = \frac{\mu_0 \pi a^3 \chi^2 H_0^2}{9kT}, \tag{2.3}$$

which is the ratio of the dipole interaction energy to the thermal energy (Promislow, Gast & Fermigier 1995). Therefore, when $\Lambda \gg 1$ the effects of Brownian motion may be ignored. Assuming the experiments of Dreyfus *et al.* (2005) were performed at $T = 300\,\mathrm{K}$, a representative value based on the reported properties of the beads and the magnitude of the applied field used is $\Lambda \approx 630$. Consequently, thermal effects may be ignored when considering the dynamics of the artificial swimmer.

2.1. *Magnetic interactions*

To resolve completely the magnetic interactions between the beads requires determining a solution to Laplace's equation for the scalar potential Φ, where $\boldsymbol{H} = -\nabla\Phi$, subject to the appropriate boundary conditions on the surface of each bead and at infinity (Jackson 1999). From this solution, the total magnetic field can be ascertained and the Maxwell stress tensor evaluated to give the interbead magnetic forces. This process is often quite cumbersome and involves providing values for the many magnetic multipoles arising from the complex interactions (Clercx & Bossis 1993). To reduce this to a tractable problem, we consider merely the interactions arising from the dipole terms. We do, however, allow the magnetic dipoles of each bead to depend on the value of the local field, not just the applied field. Accordingly, the dipole moment of particle n is given by (Jackson 1999)

$$\boldsymbol{m}_n = \frac{4}{3}\pi\chi a_n^3 \boldsymbol{H}_{tot}(\boldsymbol{Y}_n), \tag{2.4}$$

where the magnetic susceptibility $\chi = (3(\mu - \mu_0))/(\mu + 2\mu_0)$ and

$$\boldsymbol{H}_{tot}(\boldsymbol{Y}^n) = \boldsymbol{H}(t) + \sum_{q \neq n} \frac{1}{4\pi} \left(\frac{3(\boldsymbol{Y}_n - \boldsymbol{Y}_q)(\boldsymbol{Y}_n - \boldsymbol{Y}_q) \cdot \boldsymbol{m}_q}{r_{nq}^5} - \frac{\boldsymbol{m}_q}{r_{nq}^3} \right) \tag{2.5}$$

with $r_{nq} = \sqrt{(\boldsymbol{Y}_n - \boldsymbol{Y}_q) \cdot (\boldsymbol{Y}_n - \boldsymbol{Y}_q)}$. The dipole moments are found by solving the $3N \times 3N$ system of linear equations provided by (2.4) and (2.5).

After determining the dipole moments, the magnetic force on particle n is computed from

$$\boldsymbol{F}_{mag}^n = \mu_0 \nabla_{\boldsymbol{Y}_n} (\boldsymbol{m}_n \cdot \boldsymbol{H}_{tot}(\boldsymbol{Y}_n)). \tag{2.6}$$

There are no magnetic torques on the beads as the dipole moments are in the same direction as the local field for each particle:

$$\boldsymbol{\tau}_{mag}^n = \mu_0 \boldsymbol{m}_n \times \boldsymbol{H}_{tot}(\boldsymbol{Y}_n) = \boldsymbol{0}. \tag{2.7}$$

2.2. *Elastic coupling*

The chemically formed links produce elastic forces and bending moments that act to return a bent filament to its original linear configuration. This effect is captured by

treating each link as an inextensible, but flexible rod of length l. In such a description, the force and moment balance (Landau & Lifshitz 1986) for a link are

$$\frac{\mathrm{d}\boldsymbol{N}}{\mathrm{d}s} + \boldsymbol{K} = \boldsymbol{0}, \tag{2.8}$$

$$\frac{\mathrm{d}\boldsymbol{M}}{\mathrm{d}s} + \boldsymbol{t} \times \boldsymbol{N} + \boldsymbol{\tau} = \boldsymbol{0}. \tag{2.9}$$

$\boldsymbol{N}(s)$ is the resultant internal stress on a cross-section and $\boldsymbol{M}(s)$ is the moment of the internal stresses on the cross-section. Both $\boldsymbol{N}(s)$ and $\boldsymbol{M}(s)$ vary with arclength $0 \leqslant s \leqslant l$ and balance the applied forces per unit length $\boldsymbol{K}$ and torques per unit length $\boldsymbol{\tau}$. In (2.9), $\boldsymbol{t}$ denotes the vector tangent to the centreline of the link. The moment $\boldsymbol{M}$ is related to the deformation of the link through the constitutive law

$$\boldsymbol{M} = \kappa \boldsymbol{t} \times \frac{\mathrm{d}\boldsymbol{t}}{\mathrm{d}s} + C\boldsymbol{t}\frac{\mathrm{d}\Psi}{\mathrm{d}s}, \tag{2.10}$$

where κ is the bending modulus, C the twist modulus, and Ψ the twist angle.

Consider the link connecting beads $n-1$ and n. This link begins ($s = 0$) at the point $\boldsymbol{Y}_{n-1} + a_{n-1}\boldsymbol{t}_{n-1}$ on the surface of bead $n-1$ and ends ($s = l$) at $\boldsymbol{Y}_n - a_n\boldsymbol{t}_n$ on the surface of bead n as shown in figure 1(*b*). At the points of contact, the centreline of the link is taken to be perpendicular to the surfaces of the spheres corresponding to the clamped-end boundary conditions $\boldsymbol{t} = \boldsymbol{t}_{n-1}$ at $s = 0$ and $\boldsymbol{t} = \boldsymbol{t}_n$ at $s = l$. The link is inextensible and there is the constraint

$$(\boldsymbol{Y}_n - \boldsymbol{Y}_{n-1}) - a_n\boldsymbol{t}_n - a_{n-1}\boldsymbol{t}_{n-1} = \int_0^l \boldsymbol{t}\ \mathrm{d}s \tag{2.11}$$

on the components of the vector pointing from the attachment site on bead $n-1$ to that on bead n. Associated with this constraint are the force on bead $n-1$, $\boldsymbol{F}^{n-1}_{elas} = \lambda_1\boldsymbol{t}_{n-1} + \lambda_2\boldsymbol{p}_{n-1} + \lambda_3\boldsymbol{q}_{n-1}$ and the equal and opposite force on bead n, $\boldsymbol{F}^{n}_{elas} = -\boldsymbol{F}^{n-1}_{elas}$. These forces will produce opposite forces that act on the ends of the link and serve as boundary conditions for the force balance (2.8). As we do not consider any other forces ($\boldsymbol{K} = \boldsymbol{0}$) on the link, (2.8) becomes

$$\frac{\mathrm{d}\boldsymbol{N}}{\mathrm{d}s} = \boldsymbol{0} \tag{2.12}$$

and from the boundary conditions $\boldsymbol{N} = \boldsymbol{F}^{n-1}_{elas}$. Since there are no external torques on the link, $\boldsymbol{\tau} = \boldsymbol{0}$ and the moment balance (2.9) reduces to

$$\frac{\mathrm{d}\boldsymbol{M}}{\mathrm{d}s} + \boldsymbol{t} \times \boldsymbol{F}^{n-1}_{elas} = \boldsymbol{0}. \tag{2.13}$$

It remains to determine the resulting link shape by solving (2.13) with the constitutive law (2.10). Using the Euler angles $(\Phi(s), \Theta(s), \Psi(s))$ to describe the continuous deformation of the link between the two ends, the orientation of the coordinate system $(\boldsymbol{t}, \boldsymbol{p}, \boldsymbol{q})$ along the link relative to the coordinate system at $s = 0$ $(\boldsymbol{t}_{n-1}, \boldsymbol{p}_{n-1}, \boldsymbol{q}_{n-1})$ is

$$\begin{bmatrix} \boldsymbol{t} \\ \boldsymbol{p} \\ \boldsymbol{q} \end{bmatrix} = \mathscr{A}(s) \begin{bmatrix} \boldsymbol{t}_{n-1} \\ \boldsymbol{p}_{n-1} \\ \boldsymbol{q}_{n-1} \end{bmatrix}. \tag{2.14}$$

with

$$\mathscr{A}=\begin{bmatrix} \cos\Theta\cos\Phi & \cos\Theta\sin\Phi & -\sin\Theta \\ \sin\Psi\cos\Phi\sin\Theta-\sin\Phi\cos\Psi & \sin\Psi\sin\Phi\sin\Theta+\cos\Phi\cos\Psi & \sin\Psi\cos\Theta \\ \cos\Phi\cos\Psi\sin\Theta+\sin\Psi\sin\Phi & \cos\Psi\sin\Phi\sin\Theta-\sin\Psi\cos\Phi & \cos\Psi\cos\Theta \end{bmatrix}. \tag{2.15}$$

Using this expression for $\boldsymbol{t}$ in (2.10) and (2.13) and recognizing Ψ as the twist angle, we obtain the differential equations

$$\left.\begin{aligned} &C\frac{\mathrm{d}^2\Psi}{\mathrm{d}s^2}=0, \\ &\kappa\frac{\mathrm{d}^2\Theta}{\mathrm{d}s^2}+\kappa\cos\Theta\sin\Theta\left(\frac{\mathrm{d}\Phi}{\mathrm{d}s}\right)^2+C\cos\Theta\frac{\mathrm{d}\Phi}{\mathrm{d}s}\frac{\mathrm{d}\Psi}{\mathrm{d}s}=\lambda_1\cos\Phi\sin\Theta \\ &\quad+\lambda_2\sin\Phi\sin\Theta+\lambda_3\cos\Theta, \\ &\kappa\cos\Theta\frac{\mathrm{d}^2\Phi}{\mathrm{d}s^2}-2\kappa\sin\Theta\frac{\mathrm{d}\Theta}{\mathrm{d}s}\frac{\mathrm{d}\Phi}{\mathrm{d}l}-C\frac{\mathrm{d}\Theta}{\mathrm{d}s}\frac{\mathrm{d}\Psi}{\mathrm{d}s}=\lambda_1\sin\Phi-\lambda_2\cos\Phi. \end{aligned}\right\} \tag{2.16}$$

In the experiments, the length of the DNA molecules linking the beads are a fraction (10 %) of a bead's diameter (Dreyfus *et al.* 2005) and, therefore, we do not expect a large variation in the radius of curvature along the length of the link. We are then justified in considering the linearized version of (2.16):

$$C\frac{\mathrm{d}^2\Psi}{\mathrm{d}s^2}=0, \tag{2.17}$$

$$\kappa\frac{\mathrm{d}^2\Theta}{\mathrm{d}s^2}=\lambda_1\Theta+\lambda_3, \tag{2.18}$$

$$\kappa\frac{\mathrm{d}^2\Phi}{\mathrm{d}s^2}=\lambda_1\Phi-\lambda_2. \tag{2.19}$$

Finally, to obtain the shape of the link, we solve equations (2.17)–(2.19) subject to clamped-end boundary conditions

$$\left.\begin{aligned} &(\Psi,\Theta,\Phi)=(0,0,0)\text{ at }s=0, \\ &(\Psi,\Theta,\Phi)=(\Psi_n,\Theta_n,\Phi_n)\text{ at }s=l. \end{aligned}\right\} \tag{2.20}$$

The solution to (2.17) with these boundary conditions is

$$\Psi(s)=\frac{\Psi_n}{l}s. \tag{2.21}$$

The solutions to the bending equations (2.18) and (2.19) depend on the sign of λ_1 and are provided in Appendix A.

In addition to the forces $\boldsymbol{F}^{n-1}_{elas}$ and $-\boldsymbol{F}^{n}_{elas}$, the link exerts elastic torques on the particles,

$$\left.\begin{aligned} &\boldsymbol{\tau}^{n-1}_{elas}=\boldsymbol{M}(0)+a_{n-1}\left(\boldsymbol{t}_{n-1}\times\boldsymbol{F}^{n-1}_{elas}\right) \\ &\boldsymbol{\tau}^{n}_{elas}=-\boldsymbol{M}(l)-a_{n}\left(\boldsymbol{t}_{n}\times\boldsymbol{F}^{n}_{elas}\right) \end{aligned}\right\} \tag{2.22}$$

2.3. *Hydrodynamic interactions*

After determining the magnetic and elastic forces and torques on the beads, all the external forces and torques are known, and according to (2.1) and (2.2) must

be balanced by the hydrodynamic forces and torques. This establishes a mobility problem that must be solved to determine the motion of the particle phase. The low-Reynolds-number conditions reveal the linear relationship between the external forces and torques and the velocities and angular velocities of the beads

$$\begin{bmatrix} \mathscr{F}_{mag} + \mathscr{F}_{elas} \\ \mathscr{T}_{elas} \end{bmatrix} = \mathscr{R} \begin{bmatrix} \mathscr{V} \\ \mathscr{W} \end{bmatrix}, \tag{2.23}$$

where $\mathscr{F}_{mag}$ and $\mathscr{F}_{elas}$ are the $3N \times 1$ vectors containing all the information regarding the forces on all the beads. Similarly, $\mathscr{T}_{elas}$, $\mathscr{V}$ and $\mathscr{W}$ are $3N \times 1$ vectors holding all the torque, velocity and angular velocity information for all the particles respectively. The $6N \times 6N$ configuration-dependent, grand resistance matrix, $\mathscr{R}$, relates the forces and torques to the particle motion and the components of $\mathscr{R}$ must first be calculated before the linear system can be solved. Rather than perform these computations directly, the force-coupling method (FCM) (Maxey & Patel 2001; Lomholt & Maxey 2003) is used to evaluate the mobility problem in an approximate, yet accurate and efficient manner. Since fluid inertia is negligible ($Re \approx 10^{-5}$), the Stokes equations govern the flow. The particles are represented by a finite force multipole expansion taken to the level of force dipoles,

$$\nabla p - \eta \nabla^2 \boldsymbol{u} = \sum_{n=1}^{N+1} \boldsymbol{F}^n_{ext} \Delta_n(\boldsymbol{x} - \boldsymbol{Y}_n) + \sum_{n=1}^{N+1} \boldsymbol{G}^n \cdot \nabla \Xi_n(\boldsymbol{x} - \boldsymbol{Y}_n), \tag{2.24}$$

$$\nabla \cdot \boldsymbol{u} = 0, \tag{2.25}$$

where

$$\Delta_n(\boldsymbol{x}) = \left(2\pi\sigma^2_{n,\Delta}\right)^{-3/2} \mathrm{e}^{-r^2/2\sigma^2_{n,\Delta}}, \tag{2.26}$$

$$\Xi_n(\boldsymbol{x}) = \left(2\pi\sigma^2_{n,\Xi}\right)^{-3/2} \mathrm{e}^{-r^2/2\sigma^2_{n,\Xi}}. \tag{2.27}$$

The parameters $\sigma_{n,\Delta}$ and $\sigma_{n,\Xi}$ are set by matching the conditions for particle motion in Stokes flow and are related to the bead radius a_n as $\sigma_{n,\Delta} = a_n/\sqrt{\pi}$ and $\sigma_{n,\Delta} = a_n/(6\sqrt{\pi})^{1/3}$. $\boldsymbol{F}^n_{ext} = \boldsymbol{F}^n_{elas} + \boldsymbol{F}^n_{mag}$ is the total external force on bead n. The antisymmetric part of the tensor $\boldsymbol{G}^n$ is, in index notation, $G^n_{ij} = (1/2)\epsilon_{ijk}\tau^n_{elas,k}$ and the symmetric part is chosen so

$$\int \frac{1}{2}(\nabla \boldsymbol{u} + (\nabla \boldsymbol{u})^{\mathrm{T}}) \Xi_n(\boldsymbol{x} - \boldsymbol{Y}_n)\, \mathrm{d}^3\boldsymbol{x} = \boldsymbol{0}. \tag{2.28}$$

Once the flow field is found, the velocity and angular velocity of bead n are computed from

$$\boldsymbol{V}_n = \int \boldsymbol{u}(\boldsymbol{x}) \Delta_n(\boldsymbol{x} - \boldsymbol{Y}_n)\, \mathrm{d}^3\boldsymbol{x}, \tag{2.29}$$

$$\boldsymbol{\Omega}_n = \frac{1}{2} \int \boldsymbol{\omega}(\boldsymbol{x}) \Xi_n(\boldsymbol{x} - \boldsymbol{Y}_n)\, \mathrm{d}^3\boldsymbol{x}, \tag{2.30}$$

where $\boldsymbol{\omega}$ is the vorticity of the fluid. FCM preserves a consistent balance between the viscous dissipation in the flow and the rate of work by the particle phase and the external forces. It further captures the corresponding degenerate multipole contributions to the flow and includes the Faxén corrections for particle motion in a spatially varying flow field.

After computing the translational and angular velocities, we numerically integrate the equations of motion,

$$\frac{\mathrm{d}\boldsymbol{Y}_n}{\mathrm{d}t} = \boldsymbol{V}_n, \tag{2.31}$$

$$\frac{\mathrm{d}\boldsymbol{t}_n}{\mathrm{d}t} = \boldsymbol{\Omega}_n \times \boldsymbol{t}_n, \tag{2.32}$$

$$\frac{\mathrm{d}\boldsymbol{p}_n}{\mathrm{d}t} = \boldsymbol{\Omega}_n \times \boldsymbol{p}_n, \tag{2.33}$$

$$\frac{\mathrm{d}\boldsymbol{q}_n}{\mathrm{d}t} = \boldsymbol{\Omega}_n \times \boldsymbol{q}_n, \tag{2.34}$$

for each bead n using an explicit, stiffly stable second-order scheme (Karniadakis, Israeli & Orszag 1991). As the positions and orientations are updated, the inextensibility constraints for each link (2.11) are verified. As necessary, the values of $(\lambda_1, \lambda_2, \lambda_3)$ for a given link are adjusted by a penalty scheme to keep the deviation in length below the strict tolerance $2.5 \times 10^{-4} l$. With the penalty scheme, the forces are updated in an iterative fashion such that, if the resulting motion of the beads does not comply with the set of constraints, that time step is rejected and the elastic forces are modified in proportion to the deviation from the constraint. The motion is then recomputed with the new elastic forces, but for the same particle configuration. The process is repeated, if necessary, and the time step is accepted only once the constraints are satisfied.

3. Simulation results

The simulations are conducted using a set of computational units where the bead radius, a, has unit value. The filament tail is composed of $N = 15$ spheres of magnetic susceptibility $\chi = 1.0$. The length of the links connecting the beads is $l = 0.2a$ and corresponds to the length of the DNA linkages in the experiments (Dreyfus *et al.* 2005). The total length of the filament is taken to be $L = N(2a + l) - l = 32.8a$ and with the radius of the large sphere at the tethered end $R = 6.0a$, the ratio $R/L = 0.183$.

Dreyfus *et al.* (2005) examined how the scaled swimming speed, $U = V/(L\omega)$, changes with the sperm number

$$Sp = \left(\frac{4\pi\eta\omega L^4}{K_b} \right)^{1/4} \tag{3.1}$$

for different values of the magnetoelastic number

$$Mn = \frac{\pi\mu_0(\chi a H_0 L)^2}{6K_b(1 - \chi/6)(1 + \chi/12)} \tag{3.2}$$

when the swimmer is subject to the field (1.1). The sperm number is the ratio of the viscous to elastic forces and provides a measure of the magnitude of oscillation frequency. The magnetoelastic number is ratio of the magnetic forces to elastic forces and scales with the field strength squared. In the expressions for Sp and Mn we see the quantity K_b, the effective bending modulus of the filament. The value of K_b is related to the bending modulus of the link through $K_b = (2a + l)\kappa/l$. This is a result of requiring that the bending moment of a continuous filament of constant radius of curvature and length $2a + l$ be equal to that generated by a short link of length

l connecting two rigid segments each of length a if the beginning and end points in the two scenarios are coincident. The parameters Sp and Mn together with the values of h_0, χ, R/L and C/κ determine the mechanical properties of the swimmer. The experiments were conducted over the range $1 \leqslant Sp \leqslant 6.3$ for $Mn = 4.5$, 11.7 and 16 with $h_0 = 1.07 - 1.16$ and $R/L = 0.129$ or 0.246.

In the simulations, a swimmer is driven by the magnetic field (1.2) with $h_0 = 1.0$ and $C/\kappa = 1.0$. By adjusting the values of ω and H_0, the scaled swimming speed, U, is computed over the range $1 \leqslant Sp \leqslant 6$ for $Mn = 5$, 10 and 15.

Figure 2 shows the kinematics of the motion over one period for various Sp with $Mn = 10$. The resulting scaled swimming speeds over this range of Sp are provided in figure 3(a). In each case, the direction of swimming is such that the tethered end is at the rear of the swimmer as it swims 'tail first.' At low Sp, the filament tail remains aligned with the applied field, and together the tail and cell head rotate as a rigid body (figures 2a and 2b). Such a motion is reciprocal, or time-reversible, and accordingly, does not exhibit a net translation (Purcell 1977). Also, at low frequencies, there is significant motion of the large sphere at the tethered end as the swimmer pivots about a point within the tail. As the driving frequency is increased, viscous stresses become significant, causing the filament to deform into a spiral shape (figures 2c and 2d). Over this range of frequencies we see the swimming speed increase as the subsequent rotation of the spiral shape allows for the swimmer's translation through the fluid. If Sp is increased beyond the value corresponding to the peak swimming speed, the swimming speed is reduced as the amplitude of the deformation is diminished by the overwhelming viscous stresses (figures 2g and 2h). The variation of scaled swimming speed with Sp for planar actuation behaves in a similar manner (Gauger & Stark 2006).

In figure 3(a) we see that increasing Mn leads to a greater peak swimming speeds. At low Sp, the rate at which the swimming speed grows decreases with increasing Mn. This is a result of the filament tail's ability to remain straight and aligned with the field at greater field strengths. Figure 3(b) compares the scaled swimming speeds achieved from the use of the oscillating field (1.1) to those produced by the rotating field with $Mn = 10$. The scaled swimming speeds resulting from planar actuation are computed using the present methods and are consistent with those of Dreyfus *et al.* (2005) and Gauger & Stark (2006). While the swimming speeds are comparable at lower Sp, the speed of the swimmer in the planar oscillating field reaches its maximum value while that of the spiral swimmer continues to grow. The maximum speed for the swimmer in the rotating magnetic field is 60 % greater than that in the planar oscillating field. The magnitude of the rotating field (1.2) remains constant but the oscillating field (1.1) fluctuates in magnitude and on average is smaller.

From the simulations, it is observed that regardless of the value of Sp, the balance of the viscous, magnetic and elastic forces induces a corkscrew shape whose pitch and distance from the x-axis vary along the length of the filament (figure 2). The resulting shape rotates about the x-axis with the same frequency as the applied field. Such a stationary shape is also exhibited by a non-magnetic elastic filament with a torque applied to one end (Manghi, Schlagberger & Netz 2006). Although for the cases considered here a time-independent shape was exhibited by the swimmer, above a critical frequency of the applied field, this may not be the case especially if $h_0 > 1$. In this regime, the phase shift will increase in time until, eventually, the applied torque will reverse its direction leading to a reversal in the rotation of the filament (Cebers & Javaitis 2004b). This behaviour is related to that exhibited by a pair of non-magnetic particles in a ferrofluid subject to a rotating field (Helgesen, Pieranski & Skjeltorp 1990).

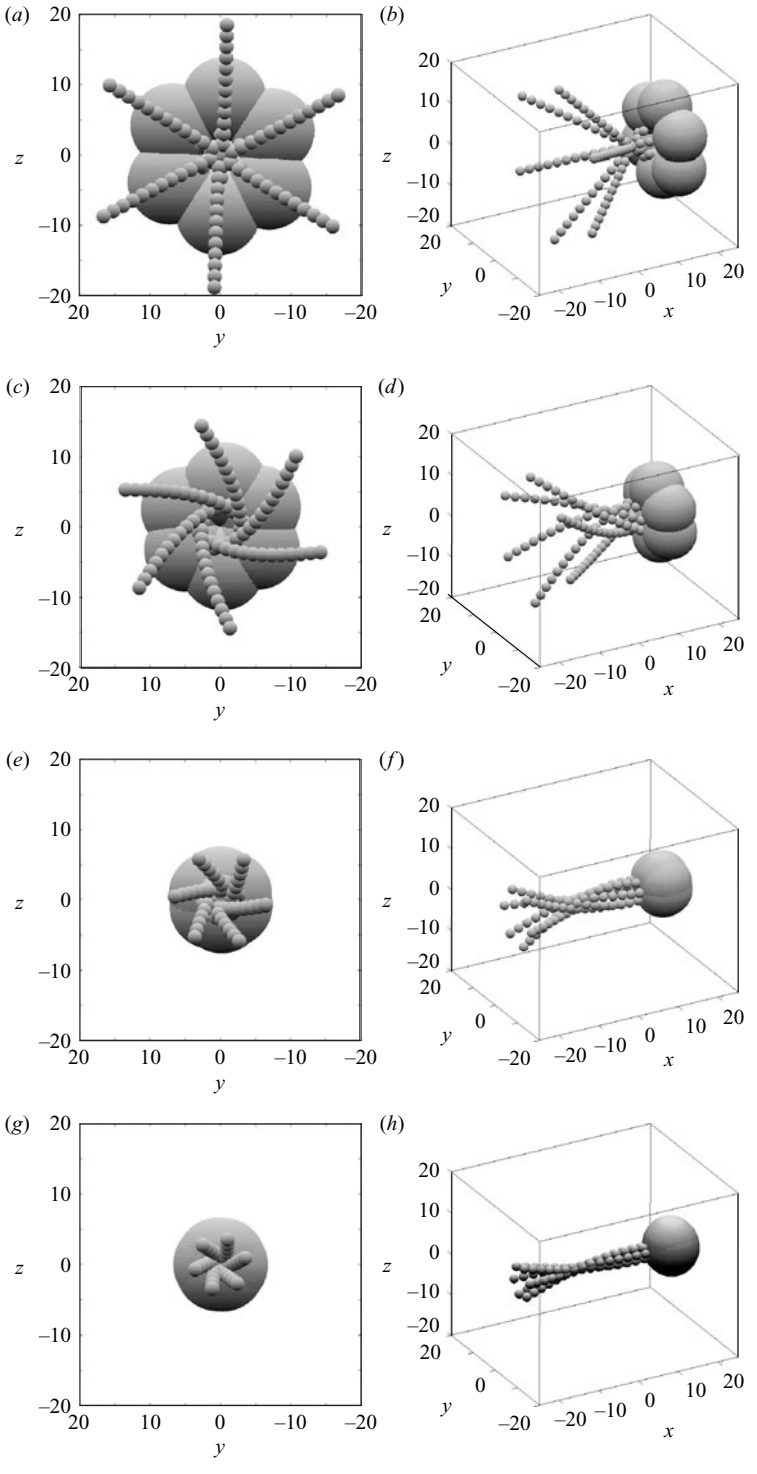

FIGURE 2. End-on and oblique views of the time-composite kinematics of the magnetic micro-swimmer over the course of one period with $R/L = 0.183$, $h_0 = 1.0$ and $Mn = 10$; (a) and (b) correspond to $Sp = 1.5$, (c) and (d) to $Sp = 3.0$, (e) and (f) to $Sp = 4.5$ and (g) and (h) to $Sp = 5.5$.

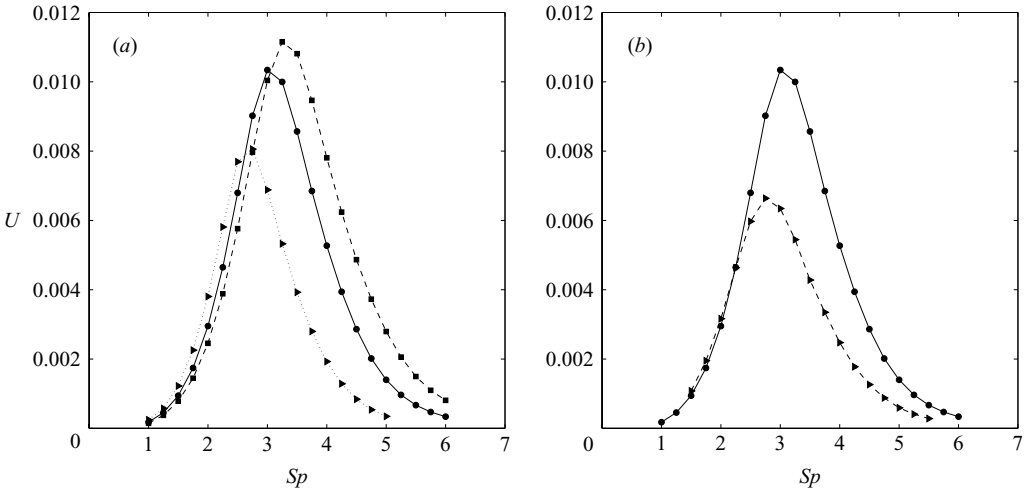

FIGURE 3. Scaled swimming speed U versus sperm number. (a) Scaled swimming speed computed using full hydrodynamic model. The dotted line with triangular markers corresponds to $Mn = 5$, the solid line with the circular markers indicates the $Mn = 10$ data, and the dashed line with the square markers is the $Mn = 15$ case. (b) Scaled swimming speed for $Mn = 10$ for different strategies. The solid line with circular markers corresponds to the rotary scheme (1.2) and the dashed line with square markers the planar strategy (1.1).

The steady-state position along the filament arclength s at time t may be described as

$$x(s,t) = \alpha(s) - Vt, \tag{3.3}$$

$$y(s,t) = -b(s)\sin(\omega t + \phi(s)), \tag{3.4}$$

$$z(s,t) = -b(s)\cos(\omega t + \phi(s)), \tag{3.5}$$

where $\alpha(s)$ is the x-component at $t = 0$, $b(s)$ is the distance from the x-axis, and $\phi(s)$ is the phase shift (Lighthill 1976). The arclength is measured relative to the free end. Differentiating in time, the resulting velocity is

$$\boldsymbol{v} = (-V, 0, 0) + (-\omega, 0, 0) \times (x, y, z). \tag{3.6}$$

Writing $\nu = \omega t + \phi(s)$, the vector tangent to the curve is given by

$$\begin{aligned}\boldsymbol{t} &= (\partial x/\partial s, \partial y/\partial s, \partial z/\partial s) \\ &= \left(\frac{\mathrm{d}\alpha}{\mathrm{d}s}, -\frac{\mathrm{d}b}{\mathrm{d}s}\sin\nu - b\frac{\mathrm{d}\phi}{\mathrm{d}s}\cos\nu, -\frac{\mathrm{d}b}{\mathrm{d}s}\cos\nu + b\frac{\mathrm{d}\phi}{\mathrm{d}s}\sin\nu\right),\end{aligned} \tag{3.7}$$

and inextensibility of the filament implies

$$\left(\frac{\mathrm{d}\alpha}{\mathrm{d}s}\right)^2 + \left(b\frac{\mathrm{d}\phi}{\mathrm{d}s}\right)^2 + \left(\frac{\mathrm{d}b}{\mathrm{d}s}\right)^2 = 1. \tag{3.8}$$

Figure 4 shows the parameters as a function of arclength over a range of Sp. In these plots, a convention is adopted where $b(s) \geqslant 0$ and $\phi(a) = \pi$ and $\alpha(a) = 0$, where $s = a$ corresponds to the centre of the bead at the free end. As Sp increases, the projection of the filament along the x-axis increases (figure 4a). Figure 4(b) shows the x-component of $\boldsymbol{t}$, $\mathrm{d}\alpha/\mathrm{d}s$ as a function of the arclength. Since $h_0 = 1.0$, $\mathrm{d}\alpha/\mathrm{d}s$ at

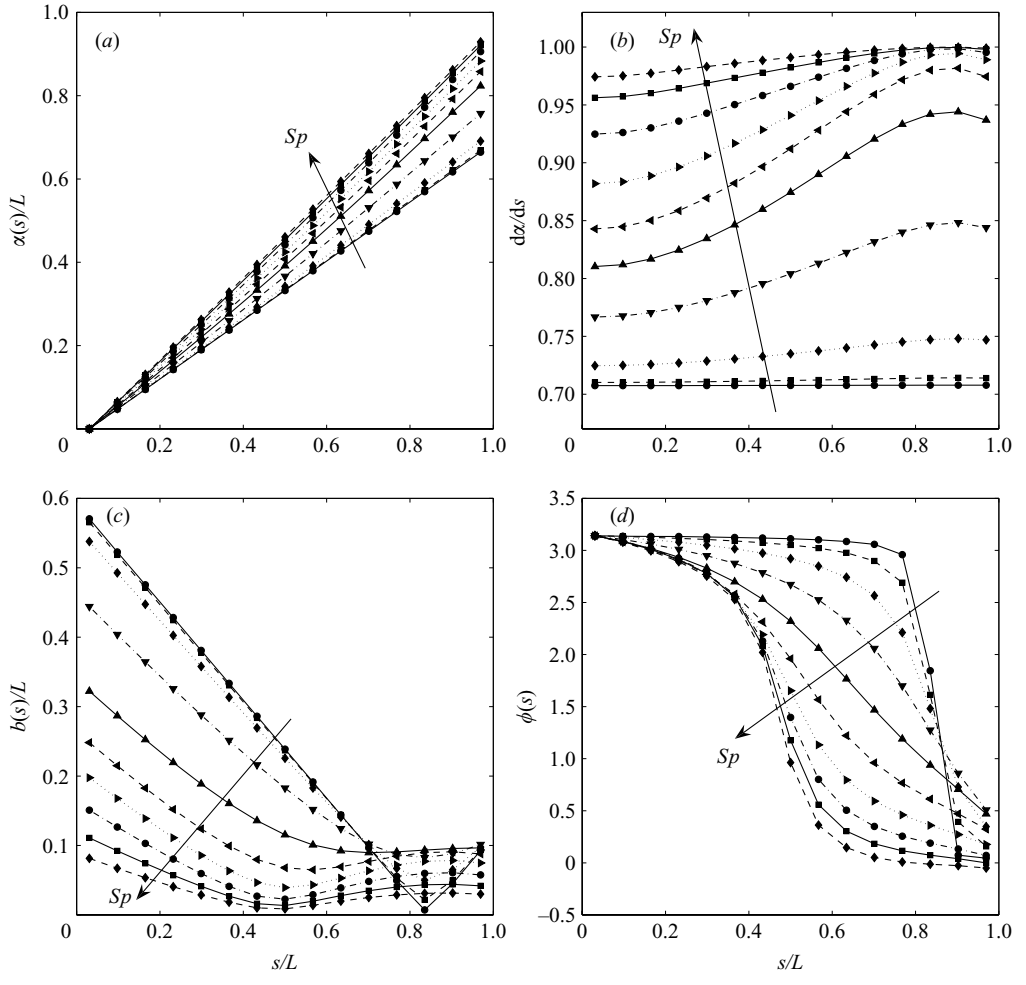

FIGURE 4. The variation of (*a*) $\alpha(s)$, (*b*) $\mathrm{d}\alpha/\mathrm{d}s(s)$, (*c*) $b(s)$, and (*d*) $\phi(s)$ with arclength s, with $Mn = 10$. The values of $\alpha(s)$ and $\phi(s)$ are given relative to those of the bead at the free end for which $s = a$, $\alpha(a) = 0$, and $\phi(a) = \pi$. The curves in each plot are for different Sp, which begin at $Sp = 1.5$ and increase by increments of 0.5 to $Sp = 6.0$.

low Sp has a nearly constant value of $\cos(\pi/4)$, which corresponds to a rigid rotation aligned with the applied field. Increasing the frequency of the applied field induces a variation in $\mathrm{d}\alpha/\mathrm{d}s$ along the length of the filament, which in the limit of very large frequencies will remain aligned with the x-axis, $\mathrm{d}\alpha/\mathrm{d}s = 1$. Similarly, in figure 4(*c*), we see the distance from the x-axis, b, decrease as the frequency is increased. Finally, in figure 4(*d*), we see that as Sp increases, a variation in the phase shift ϕ arises, which leads to the inflection point appearing at $s/L \approx 0.83$ at low Sp moving to $s/L \approx 0.5$ at high Sp.

To tie this parametrization to the observed scaled swimming speeds and swimming directions, we employ the non-dimensional version of the resistive force model which is presented in the following section. With this model and the parametrization of the motion, an expression can be derived for the scaled swimming speed by integrating the force balance (4.20) in the x-direction and applying the boundary conditions (4.25)

and (4.27). The resulting expression is

$$U = \frac{(1-\beta)\displaystyle\int_0^1 b^2 \frac{\mathrm{d}\alpha}{\mathrm{d}s}\frac{\mathrm{d}\phi}{\mathrm{d}s}\,\mathrm{d}s}{\dfrac{6\pi\eta R}{\zeta_\parallel L} + \beta + (1-\beta)\displaystyle\int_0^1 \left(\frac{\mathrm{d}\alpha}{\mathrm{d}s}\right)^2 \mathrm{d}s}, \tag{3.9}$$

where $\zeta_\parallel$ and $\beta\zeta_\parallel$ are the resistance coefficients, respectively, for motion tangent and normal to the tail. Immediately, it is clear that an anisotropic drag force ($\beta \neq 1$) is necessary to obtain a non-zero swimming speed (Becker *et al.* 2003; Lauga 2007). Other requirements include a non-zero x-component of $\boldsymbol{t}$, $\mathrm{d}\alpha/\mathrm{d}s \neq 0$, a non-zero distance from the x-axis, $b(s)$, and a variation in the phase shift, $\phi(s)$, along the length. Additionally, the dependence on b^2 of the scaled swimming speed is consistent with the results of the analysis found in Lauga (2007). From the inextensibility condition, the denominator of the above expression is positive,

$$\frac{6\pi\eta R}{\zeta_\parallel L} + 1 + (\beta-1)\left(\int_0^1 \left(\frac{\mathrm{d}b}{\mathrm{d}s}\right)^2 \mathrm{d}s + \int_0^1 \left(b\frac{\mathrm{d}\phi}{\mathrm{d}s}\right)^2 \mathrm{d}s\right) > 0 \tag{3.10}$$

as $\beta - 1 > 0$. Since $\mathrm{d}\alpha/\mathrm{d}s \geqslant 0$, $U \geqslant 0$ if $\mathrm{d}\phi/\mathrm{d}s \leqslant 0$ and by (3.3) the swimming velocity will be in the negative x-direction.

4. Resistive force model

Along with the particle-based model, we adopt a version of the continuous elastica/resistive force model presented by Roper *et al.* (2006), but extended here to allow for three-dimensional deformations. The hydrodynamics are provided by simple, approximate drag laws based on slender body theory. With such a model, we are able to generate analytic results to complement and compare with our numerical results.

The entire magnetic filament tail is treated as a flexible, inextensible rod. Accordingly, the general force and moment balance equations (2.8) and (2.9) for a massless rod apply now with $0 \leqslant s \leqslant L$. External forces and torques on the filament arise due to the presence of the surrounding fluid and applied magnetic field. Specifically,

$$\frac{\mathrm{d}\boldsymbol{N}}{\mathrm{d}s} + \boldsymbol{K}_f = \boldsymbol{0}, \tag{4.1}$$

$$\frac{\mathrm{d}\boldsymbol{M}}{\mathrm{d}s} + \boldsymbol{t}\times\boldsymbol{N} + \boldsymbol{\tau}_f + \boldsymbol{\tau}_m = \boldsymbol{0}, \tag{4.2}$$

where $\boldsymbol{K}_f$ is the translational drag force per unit length, $\boldsymbol{\tau}_f$ is the viscous torque per unit length and $\boldsymbol{\tau}_m$ is the magnetic torque per unit length on the filament.

4.1. *Hydrodynamic forces and torques*

As the filament moves through the fluid, it will experience a drag force resisting the motion. Using a resistive force theory to account for these forces gives

$$\boldsymbol{K}_f = -\boldsymbol{\zeta}\,\boldsymbol{v}, \tag{4.3}$$

where $\boldsymbol{v}$ is the filament velocity and the tensor $\boldsymbol{\zeta}$ is given by

$$\boldsymbol{\zeta} = \zeta_\parallel\left(\boldsymbol{tt} + \beta\left(\boldsymbol{I} - \boldsymbol{tt}\right)\right). \tag{4.4}$$

The drag coefficient along the tangential direction $\zeta_\parallel$ and the drag anisotropy constant β are those for a line of Stokeslets translating through fluid (Kim & Karrila 2005),

$$\zeta_\parallel = 2\pi\eta/\log(L/a) + O((\log(L/a))^{-2}), \tag{4.5}$$

$$\beta = 2, \tag{4.6}$$

where L is the length of the filament, and a is the radius of filament cross-section which is equal to the radius of a paramagnetic bead. The errors introduced by resistive force theory arise since the model assumes $a \ll L$, but more importantly $|\partial \boldsymbol{t}/\partial s| \ll 1$.

Along with the translational drag, the fluid will resist rotations of the filament about $\boldsymbol{t}$ (Wolgemuth, Powers & Goldstein 2000)

$$\boldsymbol{\tau}_f = -\zeta_r (\boldsymbol{\Omega} \cdot \boldsymbol{t}) \boldsymbol{t}, \tag{4.7}$$

with

$$\boldsymbol{\Omega} = \Omega_\parallel \boldsymbol{t} + \boldsymbol{t} \times \frac{\mathrm{d}\boldsymbol{t}}{\mathrm{d}t} \tag{4.8}$$

being the angular velocity and $\zeta_r = 4\pi\eta a^2$ the coefficient for the viscous torque.

4.2. *Magnetic torque*

In the particle-based model, the magnetic interactions between the beads produced interparticle forces, but the magnetic torque on each particle was zero. As all the magnetic forces between the beads are equal and opposite, the total magnetic force on the filament is zero. The interparticle magnetic forces will, however, produce a net torque on each segment of the filament tail. Just as the drag per unit length is determined by considering a series of Stokeslets distributed along a line, we adopt a magnetic torque model where the torque per unit length,

$$\boldsymbol{\tau} = \frac{\mu_0}{2d} \boldsymbol{m}(s) \times \boldsymbol{H}, \tag{4.9}$$

where $d = a + l/2$, corresponds to that on a line distribution of point dipoles. If the filament is straight, infinitely long and the beads comprising it are separated by $2a + l$, the dipole moment of each bead is

$$\boldsymbol{m} = \frac{4}{3}\pi a^3 \chi \left[\boldsymbol{H} + 2 \sum_{q=1}^{\infty} \frac{1}{4\pi} \left(\frac{3\boldsymbol{t}(\boldsymbol{t} \cdot \boldsymbol{m})}{8q^3 d^3} - \frac{\boldsymbol{m}}{8q^3 d^3} \right) \right]. \tag{4.10}$$

This differs from the expression derived by Roper *et al.* (2006) in that the length of the link is included in the interparticle separation distance along with the magnetic interactions of all the particles, and not just the adjacent pair. The inclusions of these details are important to make a quantitative comparison with the simulations. Due to the symmetry of the straight chain of beads and the linear relationship between the dipole moments and the applied field, we may decompose these quantities into their axial and transversal components,

$$\boldsymbol{m} = (\boldsymbol{m} \cdot \boldsymbol{t}) \boldsymbol{t} + (\boldsymbol{I} - \boldsymbol{tt}) \boldsymbol{m}, \tag{4.11}$$

$$\boldsymbol{H} = (\boldsymbol{H} \cdot \boldsymbol{t}) \boldsymbol{t} + (\boldsymbol{I} - \boldsymbol{tt}) \boldsymbol{H}. \tag{4.12}$$

On substitution into (4.10), the expression

$$\boldsymbol{m} = \frac{\frac{4}{3}\pi a^3 \chi}{1 - \frac{1}{6}\chi (a/d)^3 \zeta(3)} \boldsymbol{t}(\boldsymbol{t} \cdot \boldsymbol{H}) + \frac{\frac{4}{3}\pi a^3 \chi}{1 + \frac{1}{12}\chi (a/d)^3 \zeta(3)} (\boldsymbol{I} - \boldsymbol{tt}) \boldsymbol{H} \tag{4.13}$$

is obtained, where the Riemann zeta function prefactor

$$\zeta(3) = \sum_{k=1}^{\infty} 1/k^3 \approx 1.2.$$

The resulting applied torque (4.9) is then

$$\boldsymbol{\tau}_m = \frac{\mu_0 \pi a^6 \chi^2 \zeta(3)}{6d^4(1-(\chi/6)(a/d)^3\zeta(3))(1+(\chi/12)(a/d)^3\zeta(3))}(\boldsymbol{t}\cdot\boldsymbol{H})\boldsymbol{t}\times\boldsymbol{H}. \tag{4.14}$$

The force and moment balance are then

$$\frac{\partial \boldsymbol{N}}{\partial s} = \boldsymbol{\zeta}\boldsymbol{v} \tag{4.15}$$

$$\boldsymbol{\tau}_m + \boldsymbol{t}\times\boldsymbol{N} + \frac{\partial \boldsymbol{M}}{\partial s} = \zeta_r a^2 (\boldsymbol{\Omega}\cdot\boldsymbol{t})\boldsymbol{t} \tag{4.16}$$

The constitutive law for the stress moment is

$$\boldsymbol{M} = K_b \boldsymbol{t}\times\frac{\partial \boldsymbol{t}}{\partial s} + K_t \frac{\partial \Psi}{\partial s}\boldsymbol{t} \tag{4.17}$$

where, as before, K_b is the effective bending modulus and K_t is the effective twist modulus of the filament.

4.3. *Boundary conditions*

At the free end, $s = 0$, the forces and moments must vanish so $\boldsymbol{N} = \boldsymbol{0}$ and $\boldsymbol{M} = \boldsymbol{0}$. At the tethered end, $s = L$, the forces and moments are balanced by the translational and rotational drag of the sphere. Taking the filament as clamped to the sphere, the boundary conditions are

$$-\boldsymbol{N} - 6\pi\eta R(\boldsymbol{v} + \boldsymbol{\Omega}\times R\boldsymbol{t}) = \boldsymbol{0}, \tag{4.18}$$

$$-\boldsymbol{M} + R\boldsymbol{t}\times\boldsymbol{N} - 8\pi\eta R^3\boldsymbol{\Omega} = \boldsymbol{0}. \tag{4.19}$$

4.4. *Non-dimensional equations*

The force and moment balance equations are non-dimensionalized by introducing the barred variables such that $t = \bar{t}/\omega$, $s = L\bar{s}$, $\boldsymbol{H} = H_0\bar{\boldsymbol{H}}$, and $\boldsymbol{N} = K_b\bar{\boldsymbol{N}}/L^2$. On substituting these variables into the equations, and removing the bars, we obtain

$$\frac{\partial \boldsymbol{N}}{\partial s} = \Gamma[\boldsymbol{t}\boldsymbol{t} + \beta(\boldsymbol{I} - \boldsymbol{t}\boldsymbol{t})]\boldsymbol{v}, \tag{4.20}$$

$$\left(\frac{\zeta_r a^2}{\zeta_\parallel L^2}\right)\Gamma\Omega_\parallel \boldsymbol{t} = Cm(\boldsymbol{t}\cdot\boldsymbol{H})\boldsymbol{t}\times\boldsymbol{H} + \boldsymbol{t}\times\frac{\partial^2\boldsymbol{t}}{\partial s^2} + (K_t/K_b)\frac{\partial}{\partial s}\left(\frac{\partial\psi}{\partial s}\boldsymbol{t}\right), \tag{4.21}$$

where

$$Cm = \frac{\mu_0\pi a^6\zeta(3)(\chi H_0 L)^2}{6d^4K_b(1-(\chi/6)(a/d)^3\zeta(3))(1+(\chi/12)(a/d)^3\zeta(3))}, \tag{4.22}$$

$$\Gamma = \zeta_\parallel \omega L^4/K_b. \tag{4.23}$$

These quantities are related to Sp and Mn introduced in the experimental studies (Dreyfus *et al.* 2005) and described in the previous section. Specifically,

$$\Gamma = \frac{\zeta_\parallel Sp^4}{4\pi\eta} \tag{4.24}$$

and $Cm = 0.811Mn$. The difference between Cm and Mn is a result of the refinements in the magnetic torque model presented here.

The boundary conditions in terms of the dimensionless variables are

$$\boldsymbol{N}(0) = \boldsymbol{0}, \tag{4.25}$$

$$\boldsymbol{M}(0) = \boldsymbol{0}, \tag{4.26}$$

$$\boldsymbol{N}(1) = -Q_1 \Gamma \left(\boldsymbol{v}(1) + \boldsymbol{\Omega} \times \frac{R}{L} \boldsymbol{t}(1) \right), \tag{4.27}$$

$$\boldsymbol{M}(1) - \frac{R}{L} \boldsymbol{t} \times \boldsymbol{N}(1) = -Q_2 \Gamma \boldsymbol{\Omega}(1), \tag{4.28}$$

where

$$Q_1 = \frac{6\pi\eta R}{\zeta_\parallel L}, \tag{4.29}$$

$$Q_2 = \frac{8\pi\eta R^3}{\zeta_\parallel L^3}. \tag{4.30}$$

5. Swimming at low frequencies

With the force and moment balance equations from resistive force theory, we would like to understand how the swimming speed is affected by the values of relevant parameters. We are able to make some progress in this regard by considering the case where Γ is quite low. In this regime, the swimmer will remain closely aligned with the applied field and undergo nearly rigid rotation. Employing the resistive force hydrodynamic drag model to study this regime is appropriate since $|\partial \boldsymbol{t}/\partial s| \ll 1$. We wish to find a solution expanded, in powers of Γ, about the rigid body rotation (Wiggins & Goldstein 1998; Wiggins *et al.* 1998; Roper *et al.* 2006). From the simulations we expect the solution $\boldsymbol{t}$ to be of the form (3.7). Also, since the functions α, b and ϕ are time-independent, it suffices to find the solution at one specific time (Lighthill (1976)). Thus, at $t = 0$, the expansion is

$$\frac{\mathrm{d}\alpha}{\mathrm{d}s} = \frac{\mathrm{d}\alpha_0}{\mathrm{d}s} + \frac{\mathrm{d}\alpha_1}{\mathrm{d}s}\Gamma + O(\Gamma^2) = \frac{1}{\left(1 + h_0^2\right)^{1/2}} + \frac{\mathrm{d}\alpha_1}{\mathrm{d}s}\Gamma + O(\Gamma^2), \tag{5.1}$$

$$\frac{\mathrm{d}b}{\mathrm{d}s} = \frac{\mathrm{d}b_0}{\mathrm{d}s} + \frac{\mathrm{d}b_1}{\mathrm{d}s}\Gamma + O(\Gamma^2) = \frac{-h_0}{\left(1 + h_0^2\right)^{1/2}} + \frac{\mathrm{d}b_1}{\mathrm{d}s}\Gamma + O(\Gamma^2), \tag{5.2}$$

$$\frac{\mathrm{d}\phi}{\mathrm{d}s} = \frac{\mathrm{d}\phi_1}{\mathrm{d}s}\Gamma + O(\Gamma^2), \tag{5.3}$$

in addition to $\mathrm{d}\Psi/\mathrm{d}s = (\mathrm{d}\Psi_1/\mathrm{d}s)\,\Gamma + O(\Gamma^2)$. To avoid the discontinuity in $\mathrm{d}b_0/\mathrm{d}s$, a convention where $b(s)$ is allowed to be both positive and negative is adopted. This also removes the jump in ϕ. The scaled swimming speed (3.9) is then

$$U = \frac{(1-\beta)\dfrac{1}{\left(1 + h_0^2\right)^{1/2}} \displaystyle\int_0^1 b_0^2 \frac{\mathrm{d}\phi_1}{\mathrm{d}s}\, \mathrm{d}s}{Q_1 + \beta + \dfrac{1-\beta}{1+h_0^2}} \Gamma + O(\Gamma^2) = \bar{U}\Gamma + O(\Gamma^2). \tag{5.4}$$

From this expression, one not only sees that on deviation from a rigid body motion the swimming speed is $O(\Gamma)$, but also that it is the result of the $O(\Gamma)$ variation in the phase shift over the length of the filament. The inextensibility condition (3.8) at

$O(\Gamma)$ implies

$$\frac{\mathrm{d}\alpha_1}{\mathrm{d}s} = h_0 \frac{\mathrm{d}b_1}{\mathrm{d}s}. \tag{5.5}$$

Defining

$$b_0 = -\frac{h_0}{\left(1+h_0^2\right)^{1/2}} s + C_1$$

and noting that at $t = 0$, $\sin\nu = \phi_1\Gamma + O(\Gamma^2)$ and $\cos\nu = 1 + O(\Gamma^2)$, the expansions for the scaled filament velocity and the tangent vector are

$$\boldsymbol{v} = \boldsymbol{v}_0 + \boldsymbol{v}_1\Gamma + O(\Gamma^2) \tag{5.6}$$

$$= (0, -b_0, 0) + (-\bar{U}, 0, b_0\phi_1)\Gamma + O(\Gamma^2), \tag{5.7}$$

$$\boldsymbol{t} = \boldsymbol{t}_0 + \boldsymbol{t}_1\Gamma + O(\Gamma^2) \tag{5.8}$$

$$= \left(1/\left(1+h_0^2\right)^{1/2}, 0, -h_0/\left(1+h_0^2\right)^{1/2}\right) + \left(h_0\frac{\mathrm{d}b_1}{\mathrm{d}s}, -\frac{\mathrm{d}(b_0\phi_1)}{\mathrm{d}s}, \frac{\mathrm{d}b_1}{\mathrm{d}s}\right)\Gamma + O(\Gamma^2). \tag{5.9}$$

Since $O(1)$ rotations about $\boldsymbol{t}$ are not expected, the appropriate expansion for the dimensionless angular velocity (4.8) is

$$\boldsymbol{\Omega} = \boldsymbol{\Omega}_0 + \boldsymbol{\Omega}_1\Gamma + O(\Gamma^2) \tag{5.10}$$

$$= \left(-\frac{h_0^2}{1+h_0^2}, 0, \frac{h_0}{1+h_0^2}\right) + \left(0, -\frac{1}{\left(1+h_0^2\right)^{1/2}}\frac{\mathrm{d}(b_0\phi_1)}{\mathrm{d}s}, 0\right)\Gamma + \Omega_{\parallel,1}\boldsymbol{t}_0\Gamma + O(\Gamma^2). \tag{5.11}$$

The force balance (4.20) indicates that the resultant internal stress $\boldsymbol{N}$ is $O(\Gamma)$ to first approximation. Writing $\boldsymbol{N} = \boldsymbol{N}_1\Gamma + \boldsymbol{N}_2\Gamma^2 + O(\Gamma^3)$, the force balance at $O(\Gamma)$ is

$$\frac{\mathrm{d}N_1}{\mathrm{d}s} = -\beta b_0, \tag{5.12}$$

where $\boldsymbol{N}_1 = (0, N_1, 0)$. The general solution is

$$N_1 = \frac{\beta h_0 s^2}{2\left(1+h_0^2\right)^{1/2}} - \beta C_1 s + C_2. \tag{5.13}$$

The free-end condition (4.25) requires $C_2 = 0$, whereas the tethered-end condition (4.27) dictates that

$$C_1 = \frac{Q_1(1+R/L)+\beta/2}{Q_1+\beta}\frac{h_0}{\left(1+h_0^2\right)^{1/2}} = K\frac{h_0}{\left(1+h_0^2\right)^{1/2}}. \tag{5.14}$$

The moment balance (4.21) at $O(\Gamma)$ is

$$Cm(\boldsymbol{t}_0\cdot\boldsymbol{H})\boldsymbol{t}_1\times\boldsymbol{H} + \boldsymbol{t}_0\times\boldsymbol{N}_1 + \boldsymbol{t}_0\times\frac{\mathrm{d}^2\boldsymbol{t}_1}{\mathrm{d}s^2} + (K_t/K_b)\boldsymbol{t}_0\frac{\mathrm{d}^2\Psi_1}{\mathrm{d}s^2} = \boldsymbol{0}. \tag{5.15}$$

This expression yields the three independent equations

$$\frac{\mathrm{d}^3 b_1}{\mathrm{d}s^3} - \sigma^2\frac{\mathrm{d}b_1}{\mathrm{d}s} = 0, \tag{5.16}$$

$$\frac{\mathrm{d}^3(b_0\phi_1)}{\mathrm{d}s^3} - \sigma^2\frac{\mathrm{d}(b_0\phi_1)}{\mathrm{d}s} = N_1, \tag{5.17}$$

$$\frac{\mathrm{d}^2\Psi_1}{\mathrm{d}s^2} = 0, \tag{5.18}$$

where $\sigma^2 = (1 + h_0^2)Cm$. The third equation and the free-end moment boundary condition (4.26) imply that there is no $O(\Gamma)$ twisting, or $\mathrm{d}\Psi_1/\mathrm{d}s = 0$. The general solutions to the remaining two equations are

$$\frac{\mathrm{d}b_1}{\mathrm{d}s} = A_1 \cosh \sigma s + B_1 \sinh \sigma s, \tag{5.19}$$

$$\frac{\mathrm{d}(b_0\phi_1)}{\mathrm{d}s} = A_2 \cosh \sigma s + B_2 \sinh \sigma s - \frac{N_1}{\sigma^2} - \frac{\beta h_0}{\sigma^4 \left(1 + h_0^2\right)^{1/2}}. \tag{5.20}$$

The $O(\Gamma)$ boundary conditions at the free end $s = 0$ are

$$\frac{\mathrm{d}^2 b_1}{\mathrm{d}s^2} = 0, \tag{5.21}$$

$$\frac{\mathrm{d}^2(b_0\phi_1)}{\mathrm{d}s^2} = 0, \tag{5.22}$$

while at the tethered end $s = 1$ they are

$$\frac{\mathrm{d}^2 b_1}{\mathrm{d}s^2} = 0, \tag{5.23}$$

$$\frac{\mathrm{d}^2(b_0\phi_1)}{\mathrm{d}s^2} + \frac{R}{L} N_1 = Q_2 \frac{h_0}{\left(1 + h_0^2\right)^{1/2}}. \tag{5.24}$$

Therefore, one deduces that $A_1 = B_1 = 0$, and $\mathrm{d}b_1/\mathrm{d}s = 0$. We also have

$$B_2 = -\frac{\beta}{\sigma^3} \frac{h_0}{\left(1 + h_0^2\right)^{1/2}} K \tag{5.25}$$

$$A_2 = \frac{\beta}{\sinh \sigma} \frac{h_0}{\left(1 + h_0^2\right)^{1/2}} \left[K \left(\frac{\cosh \sigma}{\sigma^2} - \frac{1}{\sigma^2} + \frac{R}{L} \right) + \frac{1}{\sigma^2} - \frac{1}{2} \frac{R}{L} + \frac{Q_2}{\beta} \right]. \tag{5.26}$$

Before proceeding, we introduce

$$F(s) = \frac{\mathrm{d}(b_0\phi_1)}{\mathrm{d}s}, \tag{5.27}$$

$$G(s) = \int_s F(s')\,\mathrm{d}s', \tag{5.28}$$

$$H(s) = \int_s G(s')\,\mathrm{d}s', \tag{5.29}$$

so $b_0\phi_1 = G(s) + C_3$. Specifically, these functions are

$$F(s) = A_2 \cosh \sigma s + B_2 \sinh \sigma s - \frac{N_1}{\sigma^2} - \frac{\beta h_0}{\sigma^4 \left(1 + h_0^2\right)^{1/2}}, \tag{5.30}$$

$$G(s) = \frac{A_2}{\sigma} \sinh \sigma s + \frac{B_2}{\sigma} \cosh \sigma s - \frac{1}{\sigma^2} \left(\frac{\beta h_0 s^3}{6\left(1 + h_0^2\right)^{1/2}} - K \frac{\beta h_0 s^2}{2\left(1 + h_0^2\right)^{1/2}} \right) - \frac{1}{\sigma^4} \left(\frac{\beta h_0 s}{\left(1 + h_0^2\right)^{1/2}} \right), \tag{5.31}$$

$$H(s) = \frac{A_2}{\sigma^2} \cosh \sigma s + \frac{B_2}{\sigma^2} \sinh \sigma s - \frac{1}{\sigma^2} \left(\frac{\beta h_0 s^4}{24\left(1 + h_0^2\right)^{1/2}} - K \frac{\beta h_0 s^3}{6\left(1 + h_0^2\right)^{1/2}} \right) - \frac{1}{\sigma^4} \left(\frac{\beta h_0 s^2}{2\left(1 + h_0^2\right)^{1/2}} \right). \tag{5.32}$$

The force balance at $O(\Gamma^2)$ is

$$\frac{\mathrm{d}\boldsymbol{N}_2}{\mathrm{d}s} = (1-\beta)\boldsymbol{t}_0\,(\boldsymbol{t}_1\cdot\boldsymbol{v}_0 + \boldsymbol{t}_0\cdot\boldsymbol{v}_1) + \beta\boldsymbol{v}_1, \tag{5.33}$$

which may be written as

$$\frac{\mathrm{d}\boldsymbol{N}_2}{\mathrm{d}s} = (1-\beta)\boldsymbol{t}_0\left(\frac{\mathrm{d}(b_0(G(s)+C_3))}{\mathrm{d}s} + 2\frac{h_0}{\left(1+h_0^2\right)^{1/2}}(G(s)+C_3) - \frac{1}{(1+h_0)^{1/2}}\bar{U}\right) + \beta\boldsymbol{v}_1. \tag{5.34}$$

The following expressions for $\boldsymbol{N}_2 = (N_{2x}, 0, N_{2z})$ are obtained by integrating the above equation and applying the free-end boundary conditions $N_{2x} = N_{2z} = 0$. We have

$$N_{2x} = -\bar{U}s\left(\beta + \frac{1-\beta}{1+h_0^2}\right) + C_3\frac{h_0(1-\beta)s}{1+h_0^2} + \frac{1-\beta}{\left(1+h_0^2\right)^{1/2}}\left(b_0(s)G(s) - b(0)G(0) + 2\frac{h_0}{\left(1+h_0^2\right)^{1/2}}(H(s)-H(0))\right), \tag{5.35}$$

$$N_{2z} = -\bar{U}s\frac{(1-\beta)h_0}{1+h_0^2} + C_3\left(\frac{h_0^2(1-\beta)s}{1+h_0^2} + \beta s\right) + \beta(H(s)-H(0)) + \frac{h_0(1-\beta)}{\left(1+h_0^2\right)^{1/2}}\left(b_0(s)G(s) - b(0)G(0) + 2\frac{h_0}{\left(1+h_0^2\right)^{1/2}}(H(s)-H(0))\right). \tag{5.36}$$

To determine C_3 and $\bar{U}$, we apply the boundary conditions at the tethered end,

$$N_{2x}(1) = Q_1\bar{U}, \tag{5.37}$$

$$N_{2z}(1) = -Q_1\left(G(1) + C_3 + F(1)\frac{R}{L}\right). \tag{5.38}$$

We then arrive at the expression for the scaled swimming speed,

$$U = \bar{U}\Gamma + O(\Gamma^2) = \frac{h_0(\beta-1)}{(Q_1+1)(Q_1+n)\left(1+h_0^2\right)}\left(Q_1\frac{R}{L}(F(1) - (G(1)-G(0)) + (2Q_1+\beta)\left(\frac{1}{2}(G(1)+G(0)) - (H(1)-H(0))\right)\right)\Gamma + O(\Gamma^2). \tag{5.39}$$

In figure 5, the swimming speed given by (5.39) is plotted, along with the corresponding swimming speeds obtained from the simulations. In the plots, we include simulation results where the hydrodynamic interactions were truncated after the force monopole term (FCM-M) along with those including both monopoles and dipoles (FCM-MD). In both the asymptotic results and the simulations, we observe that at low Sp the scaled swimming speed U varies as Sp^4. The asymptotic prediction corresponds with the FCM-M results. This observation is attributed to the resistive force approximation being the drag associated with a line of Stokeslets. The differences in the simulation data for FCM-M and FCM-MD show the corrections from the higher-order hydrodynamic effects. In addition, the agreement between the simulations and the asymptotic solution improve as Mn increases, as the asymptotic analysis assumes that $\Gamma/Cm \ll 1$.

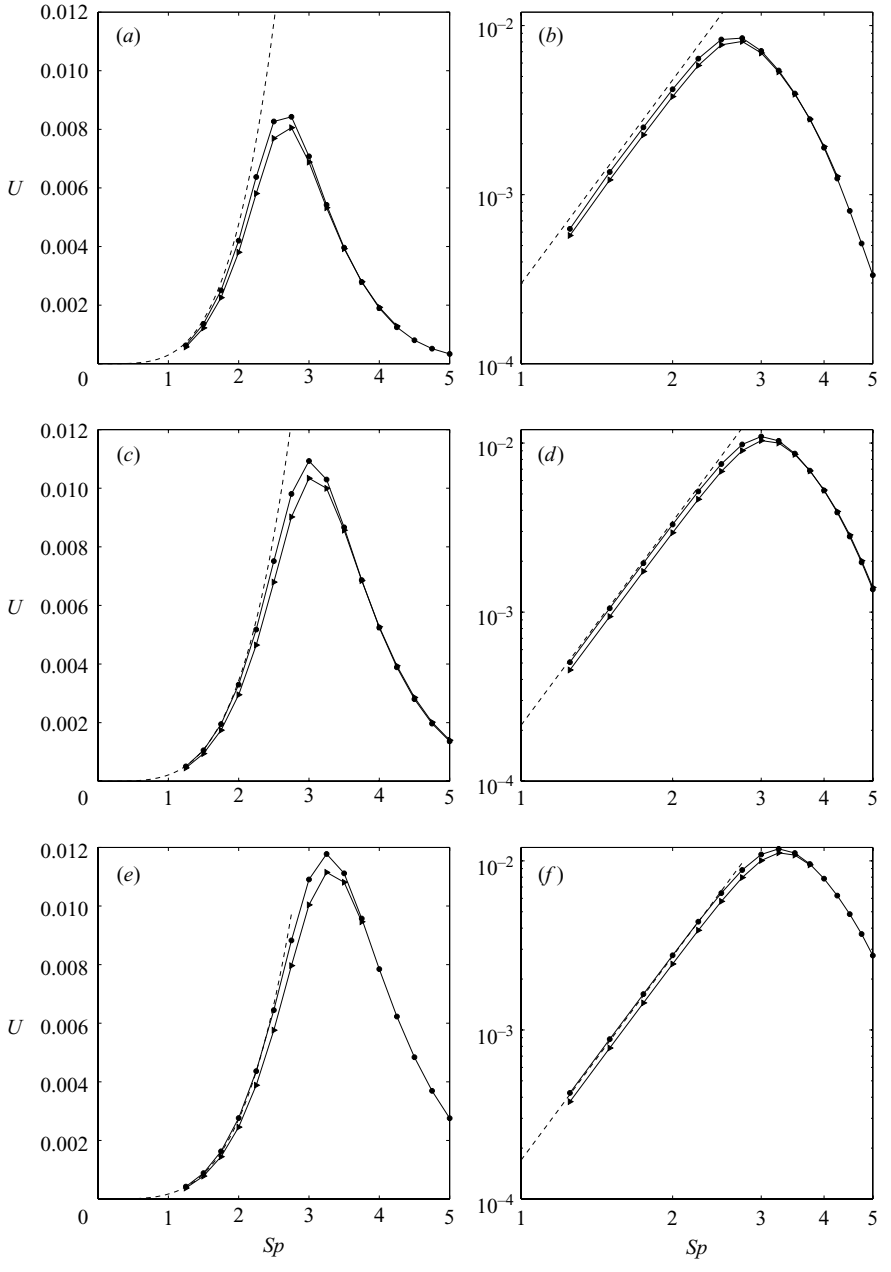

FIGURE 5. Scaled swimming speeds at low Sp for various Mn. The data are plotted in both linear–linear and log–log scales. The solid lines with the circular markers correspond to the FCM-M simulations FCM-monopole and the solid lines with the triangular markers are the FCM-MD simulations. The dashed line is the scaled swimming speed given by (5.39). In (*a*) and (*b*) $Mn = 5$ ($Cm = 4.057$), (*c*) and (*d*) $Mn = 10$ ($Cm = 8.115$), and (*e*) and (*f*) $Mn = 15$ ($Cm = 12.172$).

With the expression (5.39), we may examine how the parameters governing the magnetic forces Cm, h_0 and the geometric parameter R/L affect low Sp swimming.

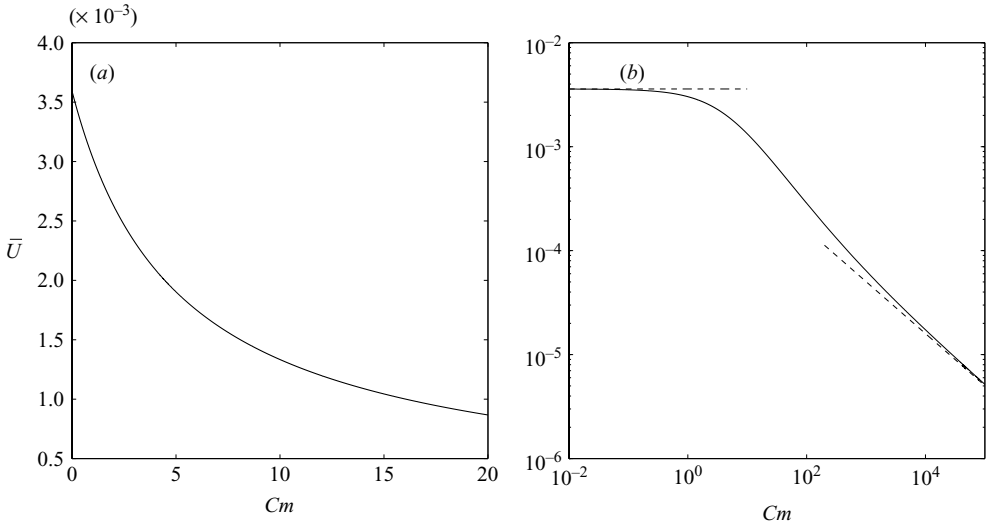

FIGURE 6. (*a*) $\bar{U}$ as a function of Cm given by (5.39). (*b*) Log–log plot of $\bar{U}$ versus Cm (solid line) including the value at $Cm = 0$ (5.40) and the asymptotic values as $Cm \to \infty$ (5.41) (dashed lines). In (*a*) and (*b*) $R/L = 0.183$ and $h_0 = 1.0$.

5.1. *Magnetic forces*

Figure 6*a* shows the coefficient in (5.39) for the scaled swimming speed, $\bar{U}$, as a function of the parameter Cm governing the relative strength of the magnetic forces. The relative amplitude of the transverse magnetic field, h_0, is set equal to 1.0. The swimming speed monotonically decreases with Cm. When $Cm = 0$, which corresponds to the absence of an applied magnetic field, the swimming speed is finite and has the value

$$\bar{U} = \frac{\beta(\beta-1)h_0^2}{(Q_1+1)(Q_1+\beta)^2\left(1+h_0^2\right)^{3/2}}\left[\left(Q_1+\frac{\beta}{2}\right)\frac{Q_1}{120}+\frac{R}{L}\frac{Q_1}{36}\left(\frac{28}{10}Q_1+\beta\right)\right.$$
$$+\left(\frac{R}{L}\right)^2\frac{Q_1}{24}(7Q_1+\beta)+\left(\frac{R}{L}\right)^3\frac{Q_1^2}{3}$$
$$\left.+\frac{Q_2}{\beta}(Q_1+\beta)\left(\frac{Q_1}{12}+\frac{Q_1}{3}\frac{R}{L}+\frac{\beta}{24}\right)\right]. \tag{5.40}$$

This result may seem alarming, but in expanding the solution it was assumed that $\Gamma/Cm \ll 1$, and therefore as $Cm \to 0$ the range of Γ over which (5.39) is valid becomes vanishingly small (Roper *et al.* 2006).

As Cm increases, the swimming speed decreases as a result of the increased magnetic torque keeping the filament aligned with the field's direction. In the limit $Cm \to \infty$,

$$\bar{U} \to \frac{\beta(\beta-1)h_0^2}{Cm^{1/2}(Q_1+1)(Q_1+\beta)^2\left(1+h_0^2\right)^2}Q_1\frac{R}{L}\left[Q_1\frac{R}{L}\left(\frac{1}{2}+\frac{R}{L}\right)\right.$$
$$\left.+\frac{Q_2}{\beta}(Q_1+\beta)\right], \tag{5.41}$$

so, $U \sim Mn^{-1/2}$. In figure 6(*b*) the value of $\bar{U}$ is plotted as a function of Cm as given by (5.39) along with the value at $Cm = 0$ and the asymptotic value $Cm \to \infty$.

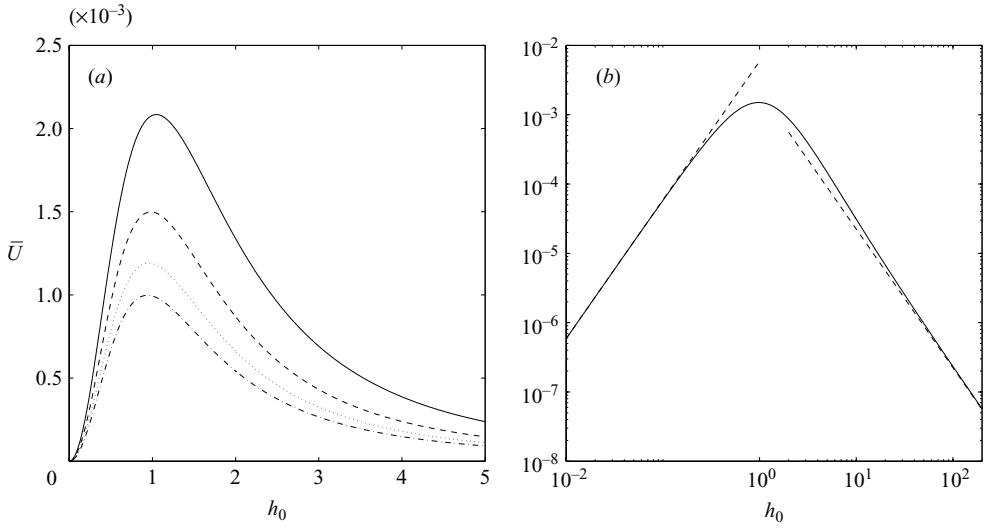

FIGURE 7. (*a*) $\bar{U}$ as a function of h_0 for $Mn = 5$ ($Cm = 4.057$) (solid line), $Mn = 10$ ($Cm = 8.115$) (dashed line), $Mn = 15$ ($Cm = 12.172$) (dotted line), and $Mn = 20$ ($Cm = 16.23$) (dash-dotted line) with $R/L = 0.183$. (*b*) Log–log plot of $\bar{U}$ (solid line) and the asymptotic values for $h_0 \to 0$ and $h_0 \to \infty$ (5.42) (dashed lines) with $Mn = 10$ and $R/L = 0.183$.

As the relative amplitude of the transverse magnetic field, h_0, increases, the swimming speed will increase to a peak value that occurs at $h_0 \approx 1$ and subsequently decays as $h_0 \to \infty$ (figure 7*a*). The limit $h_0 \to 0$ corresponds to the magnitude of the transverse field approaching zero. In this limit the swimmer will remain aligned with the x-axis, so $b(s)$, and consequently U will vanish. Since $\sigma \to \sqrt{Cm}$, the values of the functions listed in Appendix B all scale linearly in h_0. Therefore, from (5.39), we have $\bar{U} \sim h_0^2$.

At the other extreme, when $h_0 \to \infty$, the transverse field is much greater in magnitude than the constant field. In fact, the magnitude of the total field becomes unbounded. Therefore, in this limit, the swimmer will remain closely aligned with the applied field and rotate as a rigid body. Also, since the applied field is essentially localized to the yz-plane, $\mathrm{d}\alpha/\mathrm{d}s$ will be zero. For these reasons, a significant swimming speed is not expected at this limit either. To obtain the asymptotic expression, we recognize $\sigma \to h_0\sqrt{Cm}$, and as a result

$$\bar{U} \to \frac{\beta(\beta-1))}{(Q_1+1)(Q_1+n)h_0^2\sqrt{Cm}} Q_1 \frac{R}{L}\left(K\frac{R}{L} - \frac{1}{2}\frac{R}{L}\frac{Q_2}{\beta}\right). \tag{5.42}$$

This leading-order term is from $F(1)$ in (5.39), which is associated with the force balance boundary condition term $\boldsymbol{\Omega} \times \boldsymbol{Rt}$ in (4.1). In figure 7(*b*) we plot $\bar{U}$ as a function of h_0 along with the asymptotic values. The $h_0 \to 0$ asymptotic value was calculated by using $\sigma = \sqrt{Cm}$.

5.2. *Swimmer geometry*

The low-Sp swimming speed increases monotonically with R/L. In this case, the validity of the calculation is limited to situations where R/L does not exceed $R/L \sim O(1)$. Within this range, the calculation indicates that the larger cargo size increases the deformation of the filament which, in turn, produces higher swimming speeds. At large R/L, however, the drag becomes excessive and should cause the swimming

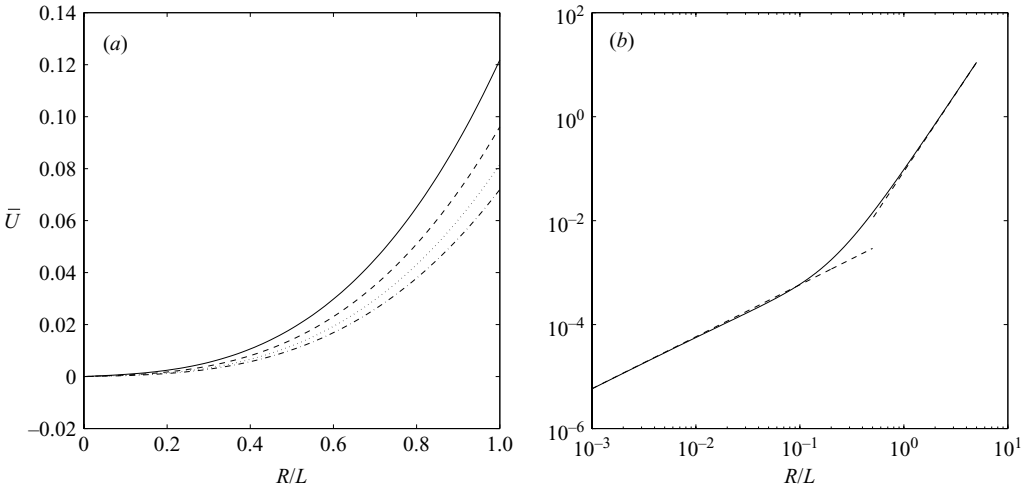

FIGURE 8. (*a*) $\bar{U}$ as a function of R/L for $Mn = 5$ (solid line), $Mn = 10$ (dashed line), $Mn = 15$ (dotted line), and $Mn = 20$ (dash-dotted line) with $h_0 = 1.0$. (*b*) Log-log plot of $\bar{U}$ (solid line) and the asymptotic values for $R/L \to 0$ (5.44) and $R/L \to \infty$ (5.46) (dashed lines) with $Mn = 10$ and $h_0 = 1$.

speed to decrease. This effect is not captured by this calculation. When $R/L = 0$ swimming is not expected since, in the absence of the sphere, the magnetic filament considered here is a symmetric body. This is recovered by the asymptotic solution. In a more general setting, however, variations in the magnetic susceptibility, χ, or in the elastic properties of the links (Roper *et al.* 2006) along the filament can produce the asymmetry in the bending wave necessary to generate a net translation in the absence of any cargo.

In the limit of $R/L \to 0$,

$$K \to \frac{1}{2} + \frac{Q_1}{2\beta}, \tag{5.43}$$

and the coefficient $\bar{U}$ for the swimming speed takes the limit

$$\bar{U} \to \frac{(\beta - 1))h_0^2}{(1 + h_0)^{3/2}} \frac{Q_1}{2} \left(\frac{1}{12\sigma^2} - \frac{1}{\sigma^4} + \frac{2}{\sigma^5} \frac{\cosh\sigma - 1}{\sinh\sigma} \right). \tag{5.44}$$

Therefore, $\bar{U} \sim R/L$. On the other hand, as $R/L \to \infty$,

$$K \to \frac{R}{L}. \tag{5.45}$$

With this value for K the limiting value for $\bar{U}$ is

$$\bar{U} \to \frac{(\beta - 1)h_0^2}{(1 + h_0)^{3/2}} \frac{Q_2(R/L)}{Q_1} \left(\frac{\cosh\sigma}{\sigma \sinh\sigma} - \frac{1}{\sigma^2} \right), \tag{5.46}$$

and thus $\bar{U} \sim (R/L)^3$.

Figure 8(*b*) shows $\bar{U}$ as a function of R/L along with the asymptotic values presented above. We see that at $R/L \approx 0.1$, the dependence begins to transition from linear to cubic. When R/L is small, the sphere's translational drag is greater than its rotational drag. Therefore, the deformation of the filament that leads to swimming is a result of the asymmetry caused by the translation of the sphere. However, once

R/L becomes large enough, the rotational drag will be larger than the translational drag, and, accordingly, the dependence of deformation associated with swimming will be $\sim (R/L)^3$.

6. Summary and conclusions

A fully three-dimensional simulation scheme has been presented that describes the dynamics of a chain of discrete paramagnetic beads bonded together by short flexible links to form a tail attached to a larger spherical particle or head. The scheme captures in detail the effects of magnetic, fluid and elastic forces within the filament. It has been demonstrated that the magnetic micro-swimmer introduced by Dreyfus *et al.* (2005) with planar actuation can be used as a model to study a corkscrew form of swimming, driven by a rotating magnetic field. In a rotating field, the swimmer will deform into a spiral shape that rotates about an axis in the direction of swimming. The kinematics of the motion were extracted and parameterized by time-independent functions describing the pitch, the distance from the axis of symmetry and the phase shift along the length of the tail. Further, the correspondence between this parameterization and the observed swimming velocity was established.

An approximate description of the motion was provided by a resistive force model in which the filament tail is treated as a continuous elastica subject to a distributed magnetic torque per unit length. An asymptotic analysis for low-frequency rotations predicted that the swimming speed grows initially as $U \sim Sp^4$. The refinements to the resistive force model described in § 4 were essential in order to match the simulation results. Once this was done, there was a good correspondence between the two for the swimming at low frequency. The asymptotic analysis further identified broadly the effects of varying the other parameters governing the magnetic field and the geometry.

At the time of writing, there has been no experimental demonstration of spiral swimming of an artificial micro-swimmer. The present results, however, indicate that such a motion is possible, and effective. Additionally, it opens the question as to what other applied fields might be devised to generate more complex dynamics exhibited by micro-organisms. For example, as the artificial swimmer will move in the direction of the constant component of the applied field, the direction of this field can be changed over time to yield a helical swimming path similar to that of sea urchin sperm during chemotaxis (Friedrich & Jülicher 2007). The manipulation and propulsion of artificial micro-swimmers with unsteady magnetic fields provide insights into the more general questions regarding swimming micro-organisms. Naturally occurring spiral swimmers such as bacteria are both force-free and torque-free, with the torque exerted by a rotating flagellum counter-balanced by the viscous torque of the counter-rotating head. The magnetic swimmer is force-free but subject to a net torque from the external field. The magnetic tail, though, deforms in response to elastic and fluid forces and thus demonstrates the response that may be characteristic of more general systems. In particular, artificial swimmers may be used to explore the complexities of swimmer–swimmer interactions and of swimming organisms near a bounding surface or in the presence of an ambient shear flow. The discrete particle description of the simulations lends itself to these situations where resistive force models may be inaccurate or too complex to analyse.

We wish to thank Professor George Karniadakis and Professor Thomas Powers of Brown University for valuable discussions during the course of this work. This work was supported by the National Science Foundation under grant CTS-0326702.

Findings and conclusions expressed here are those of the authors do not necessarily reflect the views of the funding agency.

Appendix A

The solutions to (2.18) and (2.19) subject to the boundary conditions (2.20) depend on the sign of λ_1.

A.1. $\lambda_1 = 0$

In this case, (2.18) and (2.19) reduce to

$$\kappa \frac{\mathrm{d}^2 \Phi}{\mathrm{d}s^2} = -\lambda_2, \tag{A 1}$$

$$\kappa \frac{\mathrm{d}^2 \Theta}{\mathrm{d}s^2} = \lambda_3, \tag{A 2}$$

which, after applying the boundary conditions, have solutions

$$\Phi(s) = \frac{-\lambda_2}{2\kappa}(s-l)s + \Phi_n s/l, \tag{A 3}$$

$$\Theta(s) = \frac{\lambda_3}{2\kappa}(s-l)s + \Theta_n s/l. \tag{A 4}$$

A.2. $\lambda_1 < 0$

In this situation we have

$$\kappa \frac{\mathrm{d}^2 \Phi}{\mathrm{d}s^2} + |\lambda_1|\,\Phi = -\lambda_2, \tag{A 5}$$

$$\kappa \frac{\mathrm{d}^2 \Theta}{\mathrm{d}s^2} + |\lambda_1|\,\Theta = \lambda_3, \tag{A 6}$$

which have general solutions

$$\Phi(s) = D_1 \cos(\sqrt{|\lambda_1|/\kappa}\, s) + D_2 \sin(\sqrt{|\lambda_1|/\kappa}\, s) - \lambda_2/|\lambda_1|, \tag{A 7}$$

$$\Theta(s) = D_3 \cos(\sqrt{|\lambda_1|/\kappa}\, s) + D_4 \sin(\sqrt{|\lambda_1|/\kappa}\, s) + \lambda_3/|\lambda_1|. \tag{A 8}$$

Upon applying the clamped end boundary conditions, we see

$$D_1 = \lambda_2/|\lambda_1|, \tag{A 9}$$

$$D_2 = \frac{\Phi_n - \lambda_2/|\lambda_1|\,(\cos(\sqrt{|\lambda_1|/\kappa}\, l) - 1)}{\sin(\sqrt{|\lambda_1|/\kappa}\, l)}, \tag{A 10}$$

$$D_3 = -\lambda_3/|\lambda_1|, \tag{A 11}$$

$$D_4 = \frac{\Theta_n + \lambda_3/|\lambda_1|\,(\cos(\sqrt{|\lambda_1|/\kappa}\, l) - 1)}{\sin(\sqrt{|\lambda_1|/\kappa}\, l)}. \tag{A 12}$$

A.3. $\lambda_1 > 0$

Here,

$$\kappa \frac{\mathrm{d}^2 \Phi}{\mathrm{d}s^2} - |\lambda_1|\,\Phi = -\lambda_2, \tag{A 13}$$

$$\kappa \frac{\mathrm{d}^2 \Theta}{\mathrm{d}s^2} - |\lambda_1|\,\Theta = \lambda_3. \tag{A 14}$$

The general solutions are

$$\Phi(s) = E_1 \cosh(\sqrt{|\lambda_1|/\kappa}s) + E_2 \sinh(\sqrt{|\lambda_1|/\kappa}s) + \lambda_2/|\lambda_1|, \tag{A 15}$$

$$\Theta(s) = E_3 \cosh(\sqrt{|\lambda_1|/\kappa}s) + E_4 \sinh(\sqrt{|\lambda_1|/\kappa}s) - \lambda_3/|\lambda_1|, \tag{A 16}$$

and the boundary conditions imply

$$E_1 = -\lambda_2/|\lambda_1|, \tag{A 17}$$

$$E_2 = \frac{\Phi_n + \lambda_2/|\lambda_1|\,(\cosh(\sqrt{|\lambda_1|/\kappa}l) - 1)}{\sinh(\sqrt{|\lambda_1|/\kappa}l)}, \tag{A 18}$$

$$E_3 = \lambda_3/|\lambda_1|, \tag{A 19}$$

$$E_4 = \frac{\Theta_n - \lambda_3/|\lambda_1|\,(\cosh(\sqrt{|\lambda_1|/\kappa}l) - 1)}{\sinh(\sqrt{|\lambda_1|/\kappa}l)}. \tag{A 20}$$

Appendix B

In the expression derived for the $O(\Gamma)$ swimming speed we see the values of the functions $F(s)$, $G(s)$, and, $H(s)$ at the free and tethered ends. The values of these functions are

$$F(1) = \frac{\beta h_0}{\left(1+h_0^2\right)^{1/2}}\left[\frac{1-\cosh\sigma}{\sigma^3\sinh\sigma}K + \frac{\cosh\sigma}{\sigma\sinh\sigma}\left(K\frac{R}{L} - \frac{1}{2}\frac{R}{L} + \frac{Q_2}{\beta}\right)\right.$$
$$\left. - \frac{1}{\sigma^2}\left(\frac{1}{2} - K\right) + \frac{1}{\sigma^2}\left(\frac{\cosh\sigma}{\sigma\sinh\sigma} - \frac{1}{\sigma^2}\right)\right], \tag{B 1}$$

$$H(1) - H(0) = \frac{\beta h_0}{\left(1+h_0^2\right)^{1/2}}\left[\frac{\cosh\sigma - 1}{\sigma^3\sinh\sigma}\left(K\frac{R}{L} - 2\frac{K}{\sigma^2} + \frac{1}{\sigma^2} - \frac{1}{2}\frac{R}{L} + \frac{Q_2}{\beta}\right)\right.$$
$$\left. - \frac{1}{\sigma^2}\left(\frac{1}{24} - \frac{K}{6}\right) - \frac{1}{2\sigma^4}\right], \tag{B 2}$$

$$G(1) = \frac{\beta h_0}{\sigma^2\left(1+h_0^2\right)^{1/2}}\left[K\left(\frac{R}{L} - \frac{1}{\sigma^2} + \frac{1}{2}\right) - \frac{1}{2}\frac{R}{L} - \frac{1}{6} + \frac{Q_2}{\beta}\right], \tag{B 3}$$

$$G(0) = -\frac{\beta h_0}{\sigma^4\left(1+h_0^2\right)^{1/2}}K. \tag{B 4}$$

REFERENCES

Becker, L. E., Koehler, S. A. & Stone, H. A. 2003 On self-propulsion of micro-machines at low Reynolds number: Purcell's three-link swimmer. *J. Fluid Mech.* **490**, 15–35.

Biswal, S. L. & Gast, A. P. 2003 Mechanics of semiflexible chains formed by poly(ethylene glycol)-linked paramagnetic particles. *Phys. Rev.* E **68**, 021402.

Biswal, S. L. & Gast, A. P. 2004 Micromixing with linked chains of paramagnetic particles. *Anal. Chem.* **76**, 6448–6455.

Cebers, A. 2006 Flexible magnetic filaments in a shear flow. *J. Magn. Magn. Mater.* **300**, 67–70.

Cebers, A. & Javaitis, I. 2004*a* Bending of flexible magnetic rods. *Phys. Rev.* E **70**, 021404.

Cebers, A. & Javaitis, I. 2004*b* Dynamics of a flexible magnetic chain in a rotating magnetic field. *Phys. Rev.* E **69**, 021404.

Clercx, H. J. H. & Bossis, G. 1993 Many-body electrostatic interactions in electrorheological fluids. *Phys. Rev. E* **48**, 2721–2738.

Dreyfus, R., Baudry, J., Roper, M. L., Fermigier, M., Stone, H. A. & Bibette, J. 2005 Microscopic artificial swimmers. *Nature* **437**, 862–865.

Friedrich, B. M. & Jülicher, F. 2007 Chemotaxis of sperm cells. *Proc. Natl Acad. Sci. USA* **104**, 13256–13261.

Gauger, E. & Stark, H. 2006 Numerical study of a microscopic artificial swimmer. *Phys. Rev.* E **74**, 021907.

Goubault, C., Jop, P., Fermigier, M., Baudry, J., Bertrand, E. & Bibette, J. 2003 Flexible magnetic filaments as micromechanical sensors. *Phys. Rev. Lett.* **91**, 260802.

Helgesen, G., Pieranski, P. & Skjeltorp, A. T. 1990 Dynamic behavior of simple magnetic hole systems. *Phys. Rev.* A **42**, 7271–7280.

Jackson, J. D. 1999 *Classical Electrodynamics*, 3rd edn. Wiley.

Karniadakis, G. E., Israeli, M. & Orszag, S. A. 1991 High-order splitting methods for the incompressible Navier-Stokes equations. *J. Comput. Phys.* **97**, 414–443.

Kim, S. & Karrila, S. J. 2005 *Microhydrodynamics: Principles and Selected Applications*. Dover.

Lagomarsino, M. C., Pagonabarraga, I. & Lowe, C. P. 2005 Hydrodynamic induced deformation and orientation of a microscopic elastic filament. *Phys. Rev. Lett.* **94**, 148104.

Landau, L. D. & Lifshitz, E. M. 1986 *Theory of Elasticity*, 3rd edn. Pergamon.

Lauga, E. 2007 Floppy swimming: Viscous locomotion of actuated elastica. *Phys. Rev.* E **75**, 041916.

Lighthill, J. 1976 Flagellar hydrodynamics: The John von Neumann lecture, 1975. *SIAM Rev.* **18**, 161–230.

Lomholt, S. & Maxey, M. R. 2003 Force-coupling method for particulate two-phase flow: Stokes flow. *J. Comput. Phys.* **184**, 381–405.

Lowe, C. P. 2003 Dynamics of filaments: modelling the dynamics of driven microfilaments. *Phil. Trans. R. Soc. Lond.* B **358**, 1543–1550.

Manghi, M., Schlagberger, X. & Netz, R. R. 2006 Propulsion with a rotating elastic nanorod. *Phys. Rev. Lett.* **96**, 068101.

Maxey, M. R. & Patel, B. K. 2001 Localized force representation for particles sedimenting in Stokes flow. *Int J. Multiphase Flow* **27**, 1603–1626.

Promislow, J. H. E., Gast, A. P. & Fermigier, M. 1995 Aggregation kinetics of paramagnetic colloidal particles. *J. Chem. Phys.* **102**, 5492–5498.

Purcell, E. M. 1977 Life at low Reynolds number. *Am. J. Phys.* **45**, 3–11.

Roper, M., Dreyfus, R., Baudry, J., Fermigier, M., Bibette, J. & Stone, H. A. 2006 On the dynamics of magnetically driven elastic filaments. *J. Fluid Mech.* **554**, 167–190.

Taylor, G. I. 1951 Analysis of the swimming of microscopic organisms. *Proc. R. Soc. Lond.* A **209**, 447–461.

Taylor, G. I. 1952 The action of waving cylindrical tails in propelling microscopic organisms. *Proc. R. Soc. Lond.* A **211**, 225–239.

Wiggins, C. H., Riveline, D., Ott, A. & Goldstein, R. E. 1998 Trapping and wiggling: Elastohydrodynamcis of driven microfilaments. *Biophys. J.* **74**, 1043–1060.

Wiggins, C. H. & Goldstein, R. E. 1998 Flexive and propulsive dynamics of elastica at low Reynolds number. *Phys. Rev. Lett.* **80**, 3879–3882.

Wolgemuth, C. W., Powers, T. R. & Goldstein, R. E. 2000 Twirling and whirling: Viscous dynamics of rotating elastic filaments. *Phys. Rev. Lett.* **84**, 1623–1626.

Yu, T. S., Lauga, E. & Hosoi, A. E. 2006 Experimental investigations of elastic tail propulsion at low Reynolds number. *Phys. Fluids* **18**, 091701.